Feel free to get in contact: geo.david.fernandez@gmail.com

Sedimentation and viscosity controls on forearc high growth

David Fernández-Blanco[1], Utsav Mannu[2,3], Teodoro Cassola[4], Giovanni Bertotti[1] & Sean D. Willett[3]

[1]Department of Geoscience and Engineering, Faculty of Civil Engineering and Geosciences, Delft, University of Technology, Stevinweg 1, 2628 CN, Delft, the Netherlands

[2] Department of Earth and Climate Science, IISER Pune, Dr. Homi Bhabha Road, Pashan, Pune, 411008, India

[3] Geological Institute, Swiss Federal Institute of Technology (ETH), 8092 Zürich, Switzerland

[4] Schlumberger GmbH, Ritterstrasse 29, 52072 Aachen, Germany

Abstract

Crustal rheology and surface processes strongly influence strain distribution and shape of orogenic wedges at their front but how they influence the wedge rear is still unclear. Here, we analyze the coupled control of viscosity and sedimentation on forearc high growth during advanced stages of subduction accretion. We use 2D thermo-mechanical finite element models constrained with data of the south Anatolian margin. Our simulations show that forearc highs grow as a thermally-activated viscosity drop in the lower crust induces ductile deformation and viscous flow. Initial viscosity and the amount of sediments in the forearc basin control non-linearly the occurrence and timing of the thermally-activated viscosity drop, and thus of the growth of the forearc high. High sedimentation rates result in thicker forearc basins that stabilize the subduction wedge and delay the onset of uplift in the forearc high. Low viscosities promote earlier onset of forearc high uplift and lead to larger morphological variability along the subduction margin. Increasing either sedimentation rate or viscosity may prevent forearc high formation entirely. Forearc highs grow without a backstop at a location set by slab geometry, and at an age set by wedge thermal state. Our models explain vertical motions in south Anatolia and in other accretionary margins, like the Lesser Antilles or Cascadia, during the formation of their broad forearc highs.

Keywords: *orogenic wedge; forearc; forearc basin; outer-arc high; uplift; Turkey; Central Anatolian Plateau*

Highlights

2D FEM analysis of viscosity and sedimentation influence on forearc high growth.

Forearc highs grow without backstop at an age set by accretionary flux and wedge thermal state.

High sedimentation rates lead to thicker forearc basins and later onset of the forearc high uplift.

Low viscosities lead to larger morphological variability and earlier onset of forearc high uplift.

Increasing either sedimentation rate or viscosity may prevent forearc high formation entirely.

Introduction

Orogenic wedges growing by accretion develop characteristic cross-sectional shapes that result from the balance between basal traction in the subduction thrust and gravity, as modulated by orogenic wedge rheology and internal strain (Davis *et al.*, 1983; Platt, 1986; Willett, 1992). The geometry of the wedge front is controlled by brittle deformation, and prescribed by the mechanical properties of the accreting wedge and that of its surface of accretion (Davis *et al.*, 1983; Dahlen, 1984). The geometry of the wedge rear, however, is less well understood, given its dependence on the non-linear ductile dynamics of the deeper sectors of the wedge (Pavlis & Bruhn, 1983).

Orogen rheology and surface processes markedly influence the first-order evolution of accreting orogenic wedges. Syntectonic erosion (e.g., Koons, 1990; Willett, 1999) and sedimentation (e.g., Willett & Schlunegger, 2010; Fillon *et al.*, 2013; Erdős *et al.*, 2015) affect the distribution of strain and the deformation patterns within the wedge. Higher ductility results in structures otherwise absent, like backward thrusting sequences (Smit *et al.*, 2003). How these factors and their feedbacks influence the development and evolution of topography in the wedge internal sectors is difficult to generalize and often overlooked, limiting our understanding of the dynamic interactions among surface and deep processes at orogenic scale.

Forearc systems in accretionary margins have characteristic trench-parallel structures and derived stratigraphies (Dickinson & Seely, 1979) (Fig. 1). Forearc highs are plateau-like elevated areas developing in internal regions of some, albeit not all, forearc systems, and their formation may be explained by several mechanisms. Forearc highs may form by upward terrain growth during forced mechanical accretion of material against areas with higher relative strength commonly referred to as backstops (e.g., Byrne *et al.*, 1993; Kopp & Kukowski, 2003). Under this viewpoint, the strength contrast controls the formation of the forearc high, its structure and the limits of the wedge (Kopp & Kukowski, 2003).

Alternatively, forearc highs may uplift dynamically, supported by high temperatures and heat production in the deeper sectors of large subduction wedges (e.g., Pavlis & Bruhn, 1983; Vanderhaeghe *et al.*, 2003). In this context, forearc highs may grow by thermal activation of viscosity in the lower crust, guided by sediment deposition in the forearc basin, and ductile deformation sustained by margin accretion (Fuller *et al.*, 2006a). We focus on this latter thermo-viscous mechanism, in which the forearc high growth depends on how the interplay of wedge sedimentation, viscosity and accretion influence the thermal state and ductile strain of the wedge interior (Fernández-Blanco et al., 2020).

Here, we analyze how syn-accretion sedimentation in the forearc basin and the viscous state of the subduction wedge control the thermo-viscous uplift of forearc highs. We use 2D thermo-mechanical finite element simulations that include critical wedge visco-plastic mechanics and isostatic compensation, as well as variations in sediment input, rheological behavior, and thermal conductivity. Our Base Model uses data from the Central Cyprus accretionary margin, where the thermo-viscous uplift of the forearc high has been shown (Fernández-Blanco et al., 2020). We use the Base Model to offer details on the mechanism, and then analyze the influence of sedimentation rate on thermal distribution, strain mode and localization within and under the forearc high area. We also explore the effects that variations of specific viscous parameters (A_μ, n_μ and Q) have in the development of the internal sectors of the accretionary wedge. For all simulations, we focus on the wavelength and relative age of vertical motions in the upper crust. We find that the dynamic growth of forearc highs can take place non-linearly as defined by the geometric characteristics of the wedge and can explain short-wavelength vertical motions in inland sectors of subduction wedges.

2. Forearc elements of accretionary subduction wedges

We define morphotectonic features of arc-trench regions for generic accretionary margins in nature and in simulations and relate them to elements along Central Cyprus (Fig. 1). In nature, forearcs in accretionary systems exhibit a seaward area under mechanical accretion and an inland area where a forearc basin may be disrupted by a forearc high (Dickinson & Seely, 1979) (Fig. 1A). Imbricate seaward-verging thrusts in the seaward sector increase topography landwards from the trench to the trench-slope break, where landward-verging thrusts result in landward-dipping slopes. A trench-fill basin develops above the trench and accretionary basins lay along the trench-slope region as "piggy-back" basins carried atop thrust sheets. Landward, between the trench-slope break and volcanic arc, the forearc high may divide the forearc basin into residual and intramassif basins (Fig. 1A).

In models, shear zones develop convex-up "structural highs" enclosing convex-down "topographic depressions". We identify both features with respect to the actively deforming sector of the wedge and by location along the model transect (Fig. 1B). In model pro-wedge (seaward), topographic depressions lead to the pro-wedge and wedge-top basins (DeCelles & Giles, 1996). The area of active deformation is limited landward by the structural high, and farther toward the model retro-wedge, the growth of the forearc basin sets a stable area. When present, the forearc structural high discerns forearc basins at its front and at its back, named the pro- and retro-wedge forearc basins (Fig. 1B). We use negative-alpha basin both in nature and in models to refer to a basin with a surface slope opposite to that of the wedge that remains stable and has no internal deformation, as it slides above the subduction thrust for as long as it is restricted and steadily infilled by its bounding highs (Fuller *et al.*, 2006a; Willett & Schlunegger, 2010).

First-order morphotectonic features in the current arc-trench region of Central Cyprus correlate quite simply with the elements described above (Fig. 1C). At the southern end of the overriding Anatolian plate, the northern end of the Levantine Basin may be seen

as a trench-fill basin. Northward, the Troodos Ophiolite and the piggy-back Mesaoria Basin compound the trench-slope and the Kyrenia Range is the trench-slope break. Farther north, the Cilicia Basin is a residual basin seaward of the Mut Basin, an intramassif basin within the modern Central Taurus forearc high (Fig. 1C).

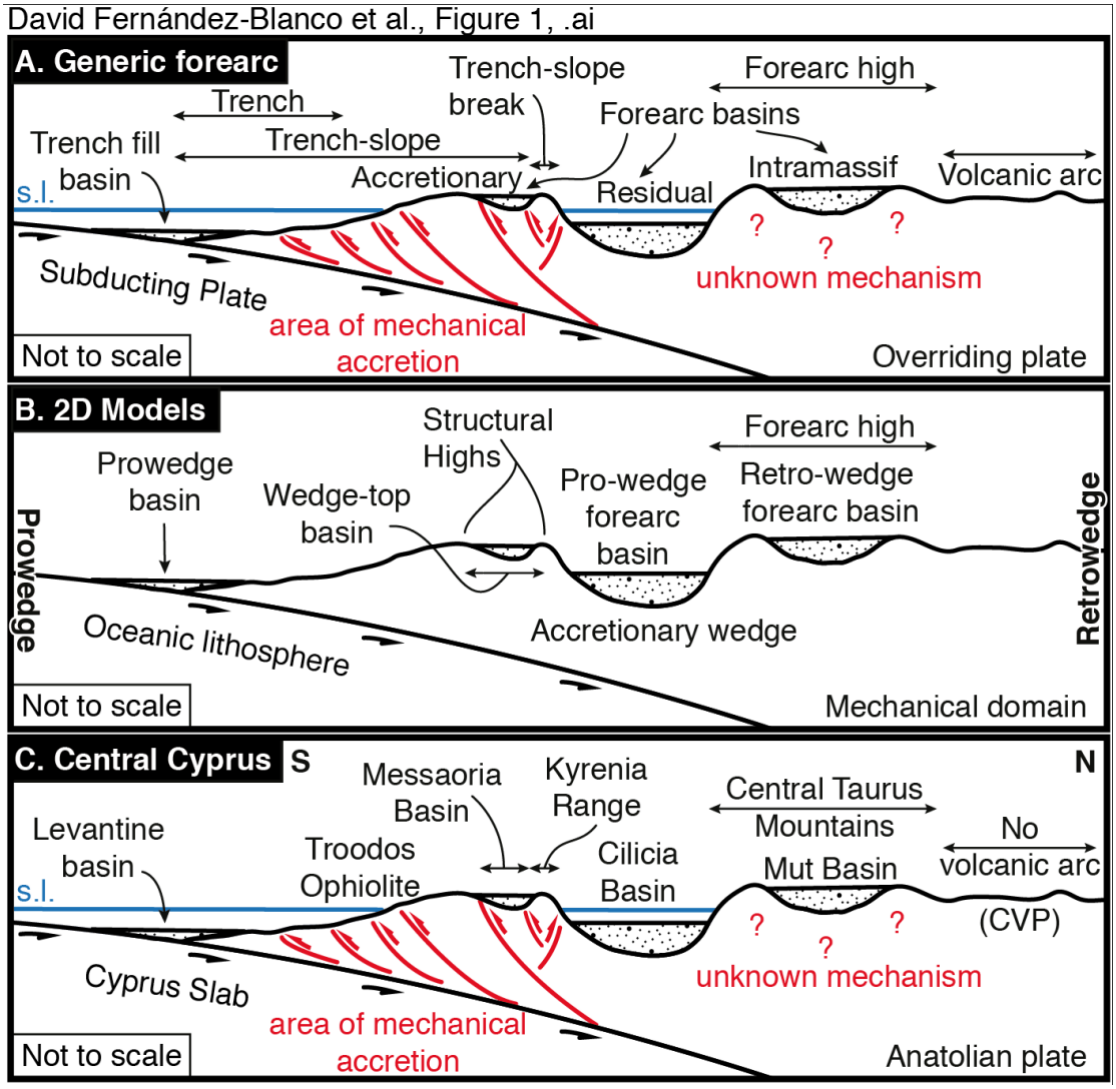

Figure 1. Accretionary margins in nature and models. *Main morphotectonic features in (A) a generic accretionary margin with forearc high, in (B) models of subduction wedge accretion, and (C) their correlation to features in Central Cyprus. For natural examples, we use original definitions by Karig & Sharman (1975) and Dickinson & Seely (1979), and for numerical models a simpler nomenclature (e.g., Fuller, 1996). "Trench-fill basin" and "accretionary forearc basin" are nature equivalents to "pro-wedge" and "wedge-top" basins in models, and the terms "residual" and "intramassif" forearc basins of Dickinson & Seely (1979) are in simulations the "landward" and "seaward" forearc basins, respectively. Correlation with elements along the Central Cyprus margin is based in Fernández-Blanco et al., 2020.*

Surface uplift of the forearc high of the Central Cyprus subduction margin spans for an area of ~200 km N-S and ~350 km E-W that led to the modern Central Taurus Mountains of South Turkey (Fig. 1). Surface uplift of the modern Central Taurus Mountains occurred in the latest Miocene (post-8Ma) and younger times (e.g., Cosentino *et al.*, 2012; Öğretmen *et al.*, 2018) with no regional fault at the surface (Fernández-Blanco *et al.*, 2019). The underlying causes behind surface uplift in South Turkey remain debated, with several studies proposing slab break-off (see Schildgen *et al.*, 2014 for a review), and more recent work suggesting crustal thickening (Meijers *et al.*, 2018) and ductile flow after thermally-activated viscosity in the lower Anatolian crust (Fernández-Blanco et al., 2020). The latter mechanism is consistent with the thick Anatolian crust and lithosphere and the presence of the Cyprus slab under the modern Central Taurus Mountains (e.g., Bakırcı *et al.*, 2012; Abgarmi *et al.*, 2017; Delph *et al.*, 2017) and the coupled, short-wavelength vertical motions reported for South Turkey and its offshore during plateau margin growth (Walsh-Kennedy *et al.*, 2014; Fernández-Blanco *et al.*, 2019).

3. Methods: Thermo-Mechanical Finite Element Models

3.1. Numerical Model Description

We used 2D thermo-mechanical finite element numerical models that simulate a transect that is comparable to the Anatolian margin in Central Cyprus, and valid for accretionary wedges elsewhere (see section 4.1). Our models use the numerical formulation by Fullsack (1995), Pope and Willett (1998) that was modified by Fuller et al. (2006a, 2006b) and now also include variations of sedimentation rate in time, strain softening and healing, and material tracking (Cassola, 2013). A detailed description of the new model formulations is provided in the supplementary material.

Our models have two coupled domains (Fig. 2). The mechanical domain represents the crust of an accreting subduction zone and its internal deformation is calculated dynamically as a response to imposed motions at its boundaries. At the base of the mechanical domain, tangential velocities drive accretion of incoming sediments. Imposed tangential velocities decrease toward the "S" point where they become zero. The "S" point represents the contact between the subducting slab and the continental Moho (Fig. 2). The thermal domain comprises the entire model and includes the mechanical domain. For a more detailed description of the model boundary conditions, the reader is referred to the supplementary material.

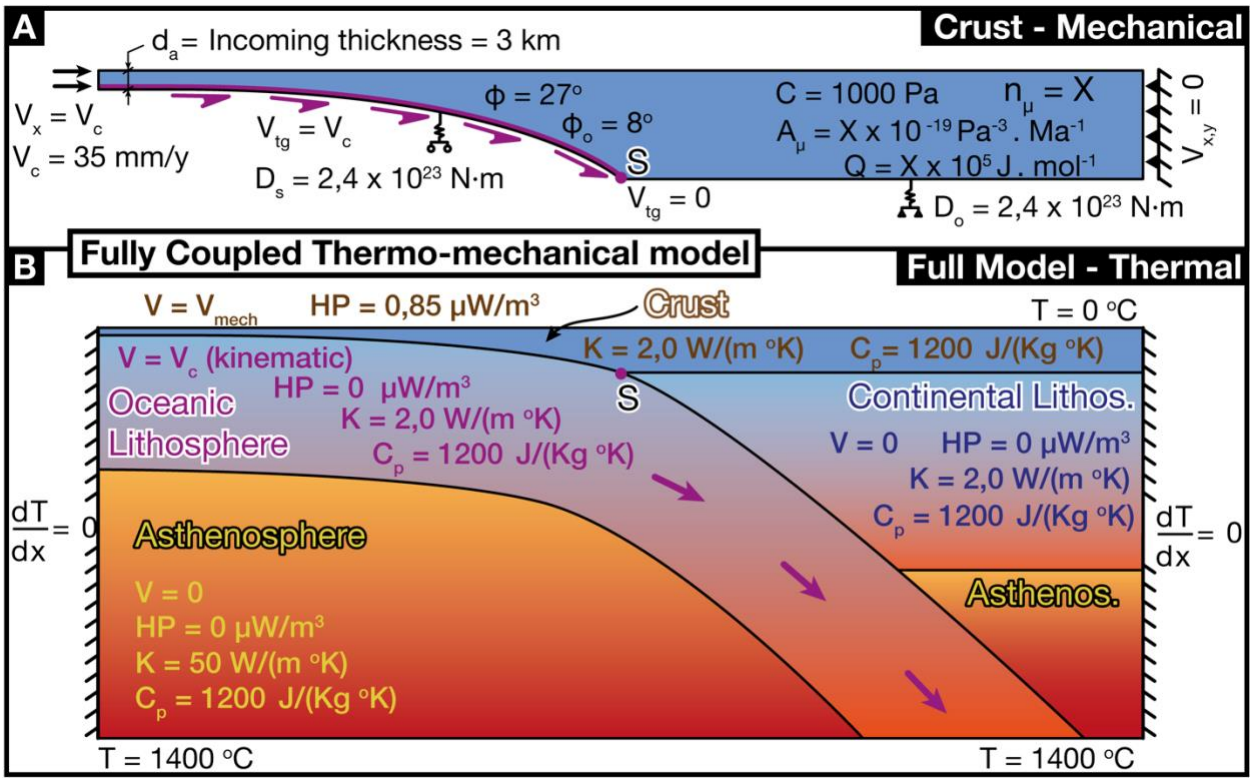

Figure 2. Model setup. *Model setup, with an indication of thermal and mechanical parameters.*

3.2 Model set up, design and parameterization

Models simulate 25 My of subduction and accretion along a transect of 550 km (Fig. 2) that we correlate with the Central Cyprus margin (Fernández-Blanco et al., 2020). We use higher than present convergence velocity, V*c* = 35 mm/yr, and a lower than present incoming material at the trench, *d* = 3 km, both constant during the model run, although present-day values for these parameters would result in a similar accretionary flux, and thus similar simulations. We justify this decision as follows. The present V*c* of 9.3+-0.3 mm/y in Cyprus (Reilinger *et al.*, 2006) is unrepresentative of the last 25 Ma, given that the underthrusting of Eratosthenes Seamount below south Cyprus results in a deceleration of the velocity or even the locking of subduction at present. The present sedimentary thicknesses observed in the East Mediterranean range between 10 km and 15 km (e.g., Makris & Stobbe, 1984) and are probably the highest in the entire Neogene, given the increasingly narrow confinement of the present-day Mediterranean and the existence of the Nile.

The subducting lithosphere is 50 My on the left of the model (pro wedge) and has a constant thickness of 70 km during the model run. The accretion of material from the model pro-wedge lead to thickening of the mechanical domain with model time. We chose an initial thickness of 30 km for the mechanical domain, which given our chosen accretionary flux, leads to a final thickness for the mechanical domain after the model run is completed that is equivalent to the thickness in nature (Fig. 3), i.e., maximum values of 45 km near the "S" point. The rest of the overriding lithosphere is 80 km thick. Flexural rigidity is set at 2.4 x 10^{23} N·m for both plates (after Fuller, 2006). Variations of flexural rigidity values of up to four orders magnitude do not produce substantial changes (e.g., Forsyth, 1985). The density of the lithosphere is 2.8 g/cc and includes the sedimentary cover. For the mantle and the overlying layer of water, we use densities of 3.3 g/cc and 1.03 g/cc, respectively.

Cohesion and internal friction angles control the mechanical strengths of our model. Cohesion *c* = 1000 Pa is set higher than expected for the crust to maintain model stability,

yet lower values do not affect the outcomes (Fuller, 2006). Both friction values, an internal friction angle φ = 27° in the crust and a friction angle φ_b = 8° at the contact between overriding and subducting plates are low in order to account for fluid pressure effects that are not accounted for explicitly, thus implying fluid pressure ratios within valid ranges at accretionary wedges (Fuller, 2006, and the references therein).

We equilibrate the thermal structure letting the thermal model run for 20 My before the onset of the crustal model. The surface temperature is 27 °C and the asthenospheric temperature at the model base is 1400 °C, and we use values for thermal conductivity of 2 and 50 W/m·°K for lithosphere and asthenosphere, respectively. Asthenospheric conductivity values are readably high to represent isothermal conditions. Heat production A = 0.85 μW/m3 (Jaupart & Mareschal, 2005) occurs only in the mechanical domain and specific heat, C_p = 1200 J/Kg·°K for both model domains.

Deposition of continental sediments with similar properties than the rest of the crust is simulated in the models. Models lack a source-to-sink mass balance; source areas are outside the models, and sediments are an extra flux of mass in the crust. Sediments fill depressions contained between structural highs to the limit of sediment availability. We use a maximum sedimentation rate to parametrize the availability of sediments. In this manner, sediment appearing at the input maximum rate fill the basins while underfill and basins remain filled if subsidence is less than such sedimentation rate. In this contribution, the maximum sedimentation rate is the effective sedimentation rate throughout most of the main forearc basin but its distal regions and smaller basins may be overfilled and have a sedimentation rate smaller than the maximum sedimentation rate. Models reproduce a synthetic stratigraphy by defining lines on the surface led by the horizontal sedimentary infill at specific time-intervals. Isochronal surfaces are subsequently tracked to understand deformation patterns since infill deposition.

3.3 Model strategy

We investigate the growth mechanics of forearc highs in accretionary subduction margins. Our models simulate a transect along any accretionary margin that runs orthogonal to the main transport direction of the incoming material, where contractional structures develop. Although valid for accretionary subduction wedges elsewhere, we chose a model set up that is comparable to the Anatolian subduction margin in Central Cyprus. For our Base Model, parameter values are set so model runs correlate to a first order with an S-N transect along the Central Cyprus subduction (see Fig. 3). Simulations are constrained by the present-day thickness and geometry of sedimentary units, and geological and plate-scale observations at the end of the simulation. However, off-section sources of material in the Anatolian margin, such as the mountainous areas to the north and northeast, and other potentially important three-dimensional effects that might occur in the area are not taken into account.

Our Base Model for Central Cyprus best represents the known time evolution of crustal vertical motions since the Early Miocene along the transect. To select our Base Model, we attended to the overall agreement of large-scale structure evolution and vertical motions through time, as well as final geometry, with particular attention to the uplifted region and domains to the south and north of it. Based on our Base Model, the values of sedimentation rate and viscosity for the parameter space studied are obtained as outcomes. We then estimate the sensitivity of the model to the influence of each parameter. In the Sedimentation Rate Suite, we study the effect of a constant maximum sedimentation rate throughout each model run, that changes among models. In the Viscosity Suite, we study the activation energy, Q, and the power-law viscosity pre-exponential and exponent, A_μ and n_μ, by systematically varying their initial values in each model run.

4. Results

4.1 Regional transect from the Mediterranean to Anatolia

We integrated tectono-sedimentary and interpreted geophysical data from on- and offshore studies in a crustal transect running from the Cyprus trench to Central Turkey (Fig. 3). See contributions and data used in the supplementary material. This integrative effort, which is complementary to that presented by Fernández-Blanco et al., 2020, allows us to constrain four key features; (a) the shape of the subducting slab and the geometry of its contact with the continental crust; (b) the overall distribution of crustal thicknesses; (c) the relative age and cutting relationships of main structures, and; (d) the position, continuity and geometry of Miocene rocks.

The African plate, comprised of the Eratosthenes continental fragment and oceanic crust northward, subducts northwards below the Anatolian thickened continental crust. The Cyprus slab subducts at angles of ~45° below the southernmost Anatolian plate and steepens at northward locations (Fig. 3A, C). The overriding Anatolian lithosphere varies from ~110 km where it contacts the slab, to ~85 km at the northern tip of the transect.

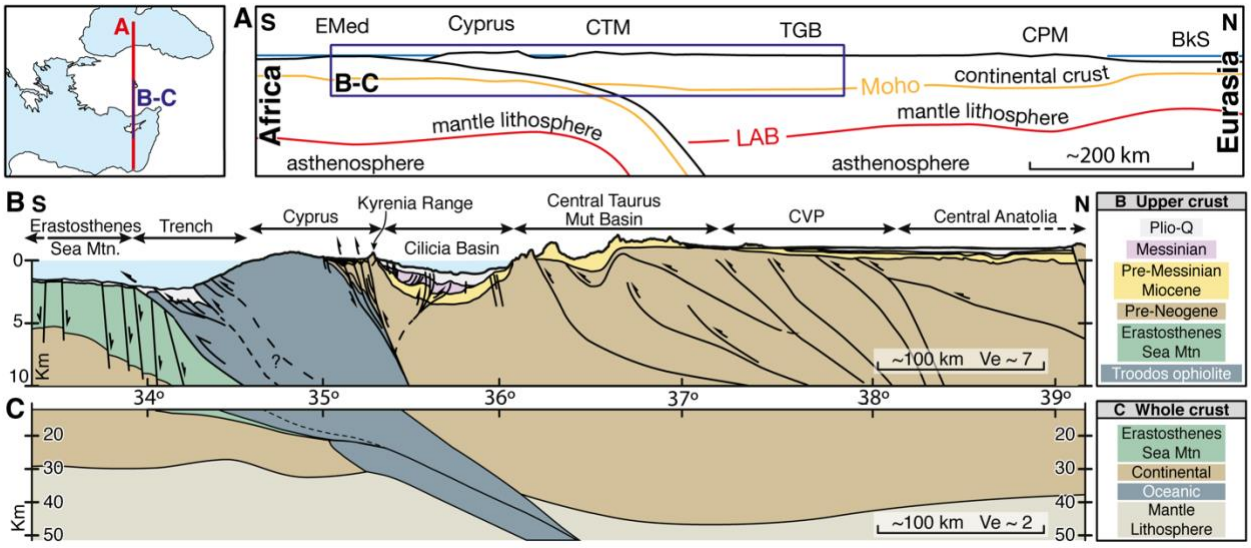

Figure 3. Transects along the Anatolian margin in Central Cyprus. *Upper-crust and crustal-scale geological transects running N-S (650 km at around 33°30' E). The transects stretch from the Levantine Basin to the Tuz*

Gölü Basin across the Cyprus arc-trench, the island of Cyprus, the Cilicia Basin, the Central Taurus Mountains, and the Central Anatolian interior. The upper-left panel is a location map. Panel A is a transect across Central Cyprus and Anatolia, simplified from Stephenson et al. (2004), that has a topo-bathymetry with 3 times vertical exaggeration. EMed = East Mediterranean; CTM = Central Taurus Mountains; TGB = Tuz Golu Basin; CPM = Central Pontides Mountains; BkS = Black Sea. Panel B is the upper sector of the transect (up to 10 km depth), shown with ~7 km of vertical exaggeration, and Panel C is the crustal cross-section for the area. These transects integrate upper crustal studies (Robertson, 1998; Stephenson et al., 2004; Calon et al., 2005a, 2005b; Çıner et al., 2008; McCay, 2010; Fernández-Blanco et al., 2013) with the interpretation of several geophysical studies (Ates et al., 1999; Mart & Ryan, 2002; Ergün et al., 2005; Koulakov & Sobolev, 2006; Özeren & Holt, 2010; Mutlu & Karabulut, 2011; Abgarmi et al., 2017; Delph et al., 2017), as detailed in Fernández-Blanco (2014). CVP = Central Volcanic Province.

Crustal thicknesses vary along the transect (Fig 3C). In the African plate and in the southern end of the transect, changes in crustal thickness can be inferred from gravimetric anomalies (Ergün *et al.*, 2005) and models of the Moho depth (Koulakov & Sobolev, 2006). Crustal thicknesses have average values of ~28 km below the Eratosthenes Seamount and are minimum (~25 km) below the trench. Geophysical models show an increase in Moho depth northward, from ~28 km at 34°30'N to >40 km at 37° N, that we relate with slab steepening (up to 40°) (Fig. 3C). The slab maintains similarly dipping until 36°30' N, where it steepens to ~60° north at ~60 km depth. This interpretation agrees with the presence of the slab ~300 km depth further north, as imaged in the section A-A of Biryol (2011). Maximum overriding crustal thicknesses of ~45 km exists near the point of contact between the African and Anatolian crust, below the Central Taurus Mountains, suggesting crustal thickening in relation to subduction. We use the interpretation of Pn tomography inferring a decrease in crustal thickness to ~35 km in the Central Anatolian interior (Mutlu & Karabulut, 2011) over gravity data (Özeren & Holt, 2010) (Fig. 3E) suggesting a crust up to ~10 km thicker.

South-verging thrusts divide the area along the transect into present-day sedimentary basins and structural highs (Fig. 3B). The thrusts become older when progressing northward along the section, and have been linked with the Cyprian subduction megathrust, directly in the south (e.g., Stephenson *et al.*, 2004; Calon *et al.*, 2005a, 2005b) and indirectly in the north (Fernández-Blanco *et al.*, 2019). They are active at the trench (e.g.,

Stephenson *et al.*, 2004), Pliocene or younger in North Cyprus (e.g., McCay, 2010), mid-Pliocene in the Cilicia Basin (Aksu *et al.*, 2005), and pre-Miocene in the Mut Basin (e.g., Çıner *et al.*, 2008). Pliocene contractional structures are seen in the Cilicia Basin, but no evidence of any Miocene or younger thrust system is known for the Mut Basin or for the transition between both basins. This transition is marked instead by monoclinal flexure along a kink-band fold that accommodates ~4 km of relative vertical displacement between coeval Miocene rocks with minimum shortening (<1 %) (Fernández-Blanco *et al.*, 2019). The aforementioned evidence is compatible with tectonic forcing from the south and northward dissipation of strain along the subduction margin.

From south to north, Miocene rocks outcrop in four different localities: the Mesaoria Basin in Cyprus, the offshore Cilicia Basin, the Mut Basin on the Central Taurus Mountains, and the Tuz Gölü Basin, in the plateau interior (Fig 3B). Basin terminations in all four Miocene basins are erosive and controlled by post-depositional tectonic contacts, with the exception of the southern margin of the Mesaoria Basin, where these rocks pinch out. The middle and upper Miocene sequences infilling these basins are composed mostly of shallow-water limestones and thus allow for a first-order estimation of vertical kinematics relative to sea level since the end of the Miocene. Rocks above pre-Miocene substratum in the asymmetrical Mesaoria Basin thin southward and are disrupted to the north by the imbricate thrusts verging south that uplift the Kyrenia Range (Calon *et al.*, 2005a, 2005b; McCay, 2010). Contrarily, the transition between rocks at ~-2 km in the Cilicia Basin and at ~2 km in the Mut Basin is a broad monocline that occurs in the absence of surface-reaching faults (Fernández-Blanco *et al.*, 2019). North of the Mut Basin, Miocene rocks in Central Anatolia are at relatively lower elevations (<1 km).

4.2 Base Model for Central Cyprus

Our Base Model uses a sedimentation rate of 0.5 mm/y and viscous parameters values of Q = 1.7 J/mol, A_μ = 2.05 Pa·n/Ma, and n_μ = 2.65. The complete list of parameter values used in our Base Model is shown in Table 1.

The time evolution of the mechanical domain of the Base Model is shown in Fig. 4. The geometry of the mechanical domain at the moment of model initiation (25 Ma) has a roughly flat topography (Fig. 4A). In the model retro-wedge (right hand of the figure), we set a topographic barrier to confine the deposition of sediments within the model and avoid model instability. The curved geometry below the mechanical domain at the model pro-wedge (left hand of the figure) is set by the down-going slab, which is not shown in the figure.

At 10 My after model onset, a large forearc (negative-alpha) basin has developed (Fig. 4B). Horizontal isochrones cover the center and retro-wedge of the model. Topography has started to develop in the model pro-wedge in relation with two shear zones, marked by warmer colors in the second invariant of the strain rate. A small asymmetric wedge-top basin develops between the shear zones that is translated toward the retro-wedge (toward the right) as the shear zones migrate. The subducting slab becomes steeper, while the base of the crust becomes more horizontal. Both factors influence the extent of strain around the "S" point, at the base of the wedge.

After 15 Ma in model time, further deepening and thickening in the forearc basin leads to increasing strain accumulation, and temperatures, at the base of the crust (Fig. 4C). As the sediments accumulate in the forearc alpha-basin, the initial development of a frontal branch of a shear zone rooted at the "S" point results in dips of the basement-basin contact toward the model pro-wedge. Farther in the model pro-wedge, the wedge-top basin migrates towards the retro-wedge and the shear zones become wider and more pronounced. Another wedge-top basin starts to develop in the model pro-wedge.

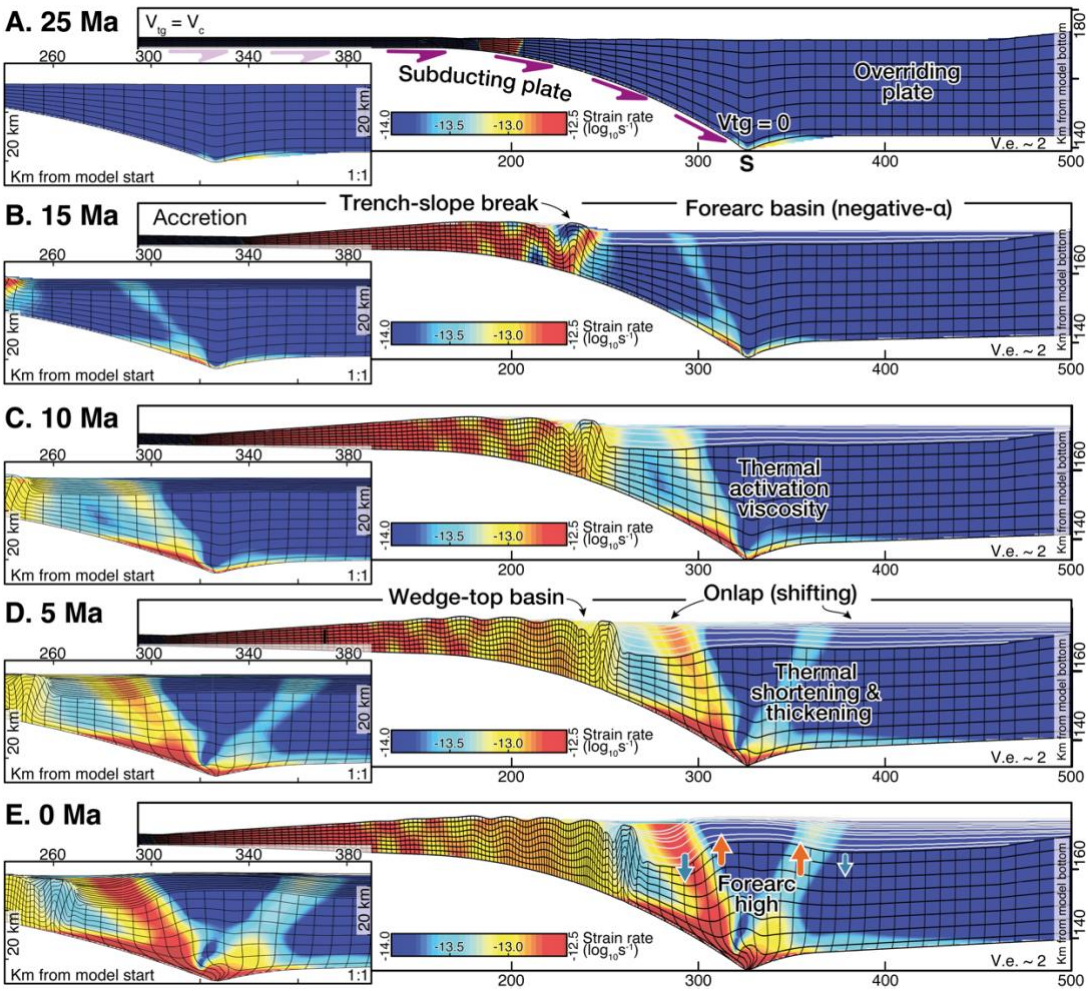

Figure 4. Base Model. *Mechanical model evolution in time steps, with zoom-ins into the area where the forearc high develops. Times represented are, from top to bottom: 25Ma, 15Ma, 10Ma, 5Ma, and present. The individual lines on top of the basement represent isochrones and should reflect the overall geometric relationships expected for strata.*

Preferred Numerical Model for Central Cyprus		
Mechanical Model		
Parameter	**Description**	**Value**
ρ_c	Lithospheric density	2800 kg/m^3
ρ_m	Mantle density	3300 kg/m^3
ρ_w	Water density	1030 kg/m^3
ϕ	Internal friction angle	27°
ϕ_b	Friction angle between subducting and overriding plate	8°
c	Cohesion	1000 Pa
D	Flexural rigidity	2.4 x 10^{23} N·m
S_α	Slab angle at S point	40°
v_c	Convergence velocity	35 mm/y
h	Sediment thickness in the subducting plate	3 km
Sed_r	Sedimentation rate	0.5 mm/y
Thermal Model		
Parameter	**Description**	**Value**
H_{sl}	Thickness of the subducting lithosphere	70 km
H_{ol}	Thickness of the overriding lithosphere	80 km
Ma_{lith}	Age of the subducting lithosphere	50 Ma
t_{runup}	Thermal model run-up	20 My
$K_{l,a}$	Thermal conductivity (lithosphere, asthenosphere)	2.0, 50.0 W/(m·°K)
T_s	Surface temperature	5 °C
T_a	Asthenosphere temperature	1400 °C
A	Heat production	0.85 μW/m^3
c	Specific heat	1200 J/Kg·°K
A_μ	Power-law viscosity coefficient	2.05 Pa^{-n}/Ma
n_μ	Power-law viscosity exponent	2.65
Q	Activation energy	1.7 J/mol

Sedimentation Rate Model Suite (variations constant per model)	
Model	**Sedimentation rate (mm/y)**
Standard	0.5
Sr1-to-Sr14	0 to 1.3 (Δ0.1)

Viscosity Model Suite (values at onset of model)			
Model	**Power-law viscosity**		**Activation Energy**
	A_μ (Pa^{-n}/Ma)	**n_μ**	**Q (J/mol)**
Preferred Model	2.05	2.65	1.7
A1-to-A7	0.05 to 4.15 (Δ0.7)	2.65	1.7
n1-to-n7	2.05	2.35 to 2.95 (Δ0.1)	1.7
Q1-to-Q7	2.05	2.65	1.4 to 2.0 (Δ0.1)

Table 1. *Values of the main parameters used in the Base Model and their parameterization for the suites of viscosity and sedimentation rate.*

At 20 Ma, two shear zones branch out from the "S" point and produce a broad uplifting bulge above it, in the central-right area of the model (Fig. 4D). The shear zones delimit the uplifted area of the forearc high, which dips gently toward the left-hand side of the model. The basement further tilts pro-wedge ward (left), and isochrones mark the onset and development of a monoclinal fold. Overall, horizontal isochrones on top of the bulge transition to isochrones dipping away from the bulge to its sides creating a broad anticlinorium. Onlap relationships take place on both sides of the bulge with larger angles in the model pro-wedge.

In the last 5 Ma, the system evolves in a self-similar manner (Fig. 4E). The bulge divided the forearc basin into a pro- and retro-wedge sub-basins sea- and land-wards respectively, and further develops the onlap relationships to its sides. The deflection of the slab proceeds toward higher angles (~40°) at the "S" point and the base of the wedge has smaller angles farther toward the retro-wedge. The basement of the pro-forearc basin deepens while uplift continues in the forearc high. An area with low values in the second invariant of strain rate develops in the uppermost ~5 km of the forearc high.

4.3 Sedimentation Rate Model Suite

Sedimentation in the models is "fill-to-spill" and areas between structural highs that are capable of accommodating sediments are filled to capacity. In doing this, we assume the availability of sufficient sediment throughout the model run. We set each model with a different sedimentation rate that remains constant throughout the model run (Table 1 and Fig. 5), and vary the sedimentation rate for different models.

Models show that as sedimentation rate increases, the strain becomes greater in and around the "S" point and is distributed in shear zones to its sides. The subducting lithosphere becomes steeper toward the model retro-wedge while the deflection of the base of the crust increases toward the "S" point. This leads to an "S" point that increasingly subsides with

increasing sedimentation (in a global reference frame). However, this is not the case if we use the position of the "S" point or that of a static sea level as a reference frame. Starting from the model with no sedimentation, models with higher sedimentation rates produce larger surface uplift. If sedimentation rates continue to increase, surface uplift eventually decreases until it reaches a threshold, after which surface uplift becomes larger again.

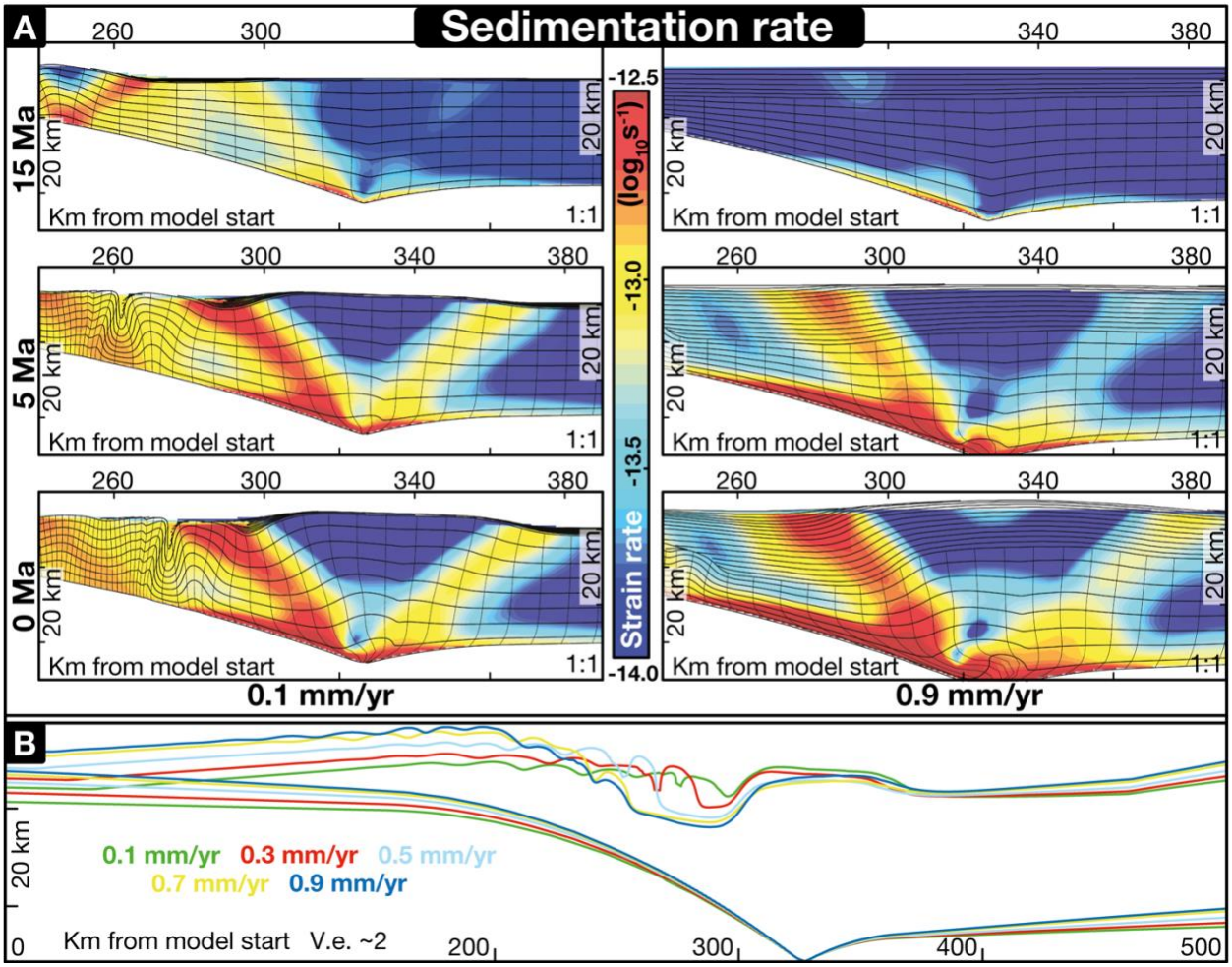

Figure 5. Variations in sedimentation rates. *Forearc high development with changes in sedimentation rates. A) The figure shows 15 Ma, 5 Ma, and 0 Ma snapshots of an inset of the model where the forearc high develops, for the models with 0.1 mm/y (left column) and 0.9 mm/y (right column). B) Line trace of the bottom of the crust and top of the basement in models with changes in sedimentation rates after a complete run. We fix the "S" point as a reference to compare models.*

As sedimentation rates increases, thicker forearc basins develop that tend to stabilize the margin and translate deformation towards the basin margins and farther away. This leads to a surface uplift that becomes smaller (Fig. 5) and eventually halts. The uplifted region dynamically supported above the thermally-activated viscosity becomes broader, and the points of maximum uplift and maximum depocenter move landward. Similarly, vertical displacements occur more gradually. This is recorded as angular discordances in basin chronolines, showing onlap relationships in models with faster forearc high growth. Increasing sedimentation rate also results in relative vertical displacements between subsided and uplifted areas that are overall consistently larger and occur in narrower (horizontally shorter) distances, i.e. larger amplitudes in the main subsidence-uplift pair (forearc high - pro-basin).

With low sedimentation rates, the initial forearc basin is thin and imposes no restrictions to forearc high surface uplift, which occurs earlier with respect to model onset, i.e. forearc high is older, and both downward/upward vertical motions take place over shorter periods. In general, with lower sedimentation rates the margin is more susceptible to the influence of the other parameters; for example, the incoming sediment at the trench markedly dominates the structural evolution of the margin, developing sharper shear zones that migrate toward the retro-wedge of the model faster and structural highs and lows that are larger in amplitude.

4.4 Viscosity Model Suite

The relationship between stress and the rate of deformation is modelled by the power-law viscosity equation:

$$D_{ij} = A_{\mu}\sigma_{ij}^{n_{\mu}} exp\left(\frac{-Q}{RT}\right)$$

where A_μ and n_μ are constants dependent on the material, Q is the activation energy, R is the molar gas constant, and T is the temperature. Table 1 shows the range of parameter values explored.

The pre-exponential viscosity parameter A_μ affects the amount of relative differential motion between the subsiding and the uplifting sectors of the forearc high and the age of the motions. Within the parameter range explored (Table 1), lower values produce a deeper initial forearc basin and delays, with relation to our Base Model, the time of formation of the (subsiding) forearc high. Forearc high growth cannot counteract the primary subsidence signal (Fig. 6). Subsidence in the initial forearc basin decelerates with time until the formation of the structural high leads to accelerating subsidence in the pro-basin and protracted decelerating subsidence in the retro-basin. Higher values of A_μ result in the rise of pronounced forearc high that develop in relation to broader shear zones, i.e. more diffuse strain, and at earlier times than our Base Model. Forearc high formation outpaces the primary subsidence signal imposed by sedimentation and surface uplift in the forearc high area is eventually larger than the subsidence recorded since forearc basin onset (Fig. 6). The rate of the motions after forearc high development accelerates with time in both forearc high and pro-basin, resulting in differential motions that become larger with time in the forearc high pro-wedge, contrarily to its retro-wedge, where the rate of subsidence remains roughly constant (Fig. 6).

The parameter n_μ exerts a control on the age, wavelength, and rate of the relative differential motions in the forearc high area, as it does on strain diffusion, in a similar manner than A_μ. Lower values of n_μ within the parameter spectrum studied (Table 1) result in the onset and protracted development of the initial forearc basin that thickens at a decelerating rate of subsidence (Fig. 7). The protracted growth of the initial forearc basin renders difficult the surface uplift of the forearc high, which cannot outpace subsidence. Higher values of n_μ produce an early uplift at older times than our Base Model. The forearc high forms soon after

the model onset, dividing an underdeveloped initial forearc basin. Uplift rates accelerate with time in the forearc high and its width remains roughly constant (Fig. 7). While the subsidence rates in the pro-wedge basin initially accelerate and then slow down at younger times, the retro-basin records the opposite trend in subsidence rates, with an older deceleration and a younger acceleration (Fig. 7).

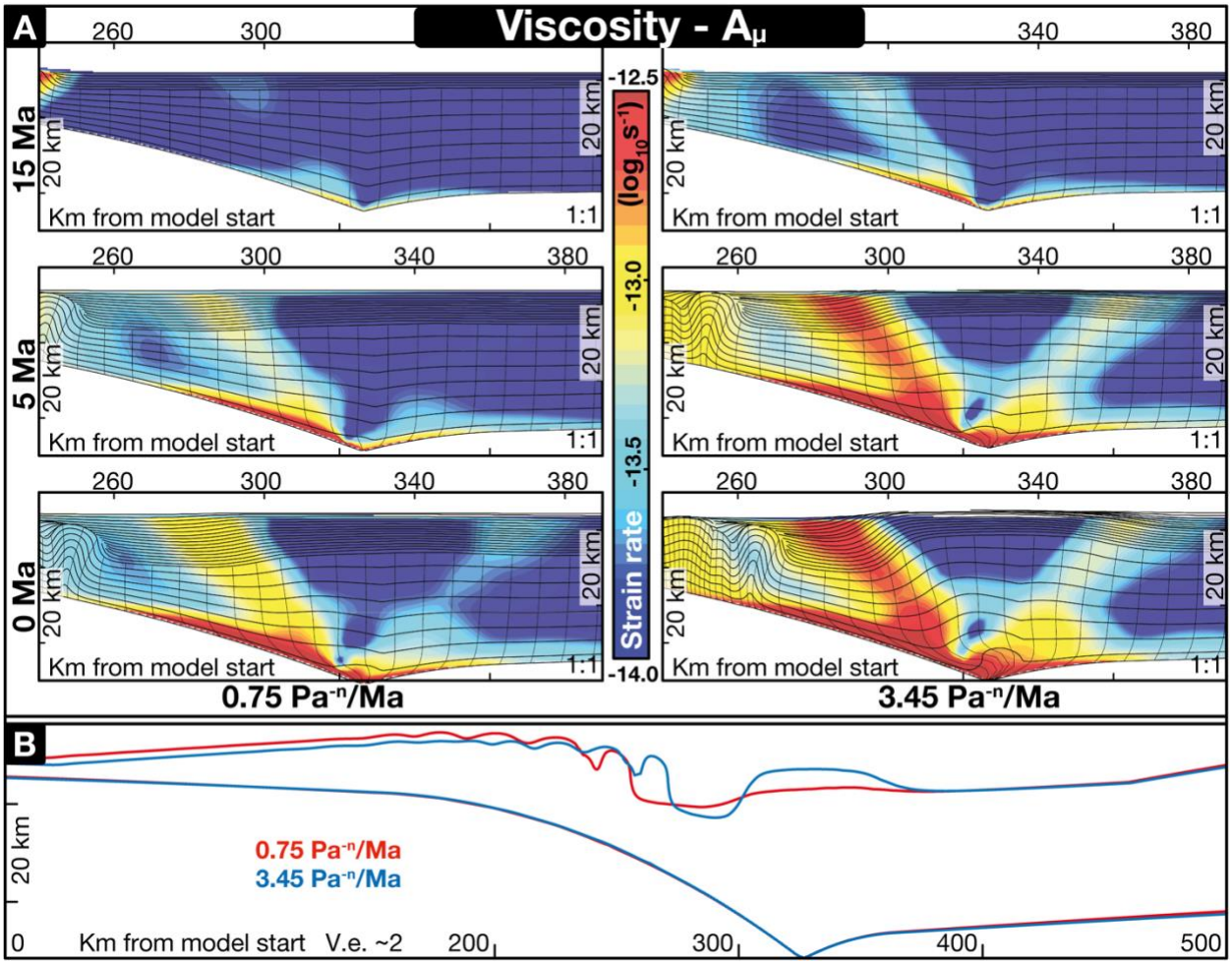

Figure 6. Variations in Aμ. *Forearc high development with changes in the viscosity pre-exponential parameter Aμ. A) The figure shows 15 Ma, 5 Ma, and 0 Ma snapshots of an inset of the model where the forearc high develops, for the models with 0.75 Pa-n/Ma (left column) and 3.45 Pa-n/Ma (right column). B) Line trace of the bottom of the crust and top of the basement in models with changes in the value of the viscosity parameter Aμ after a complete run. We fix the "S" point as a reference to compare models.*

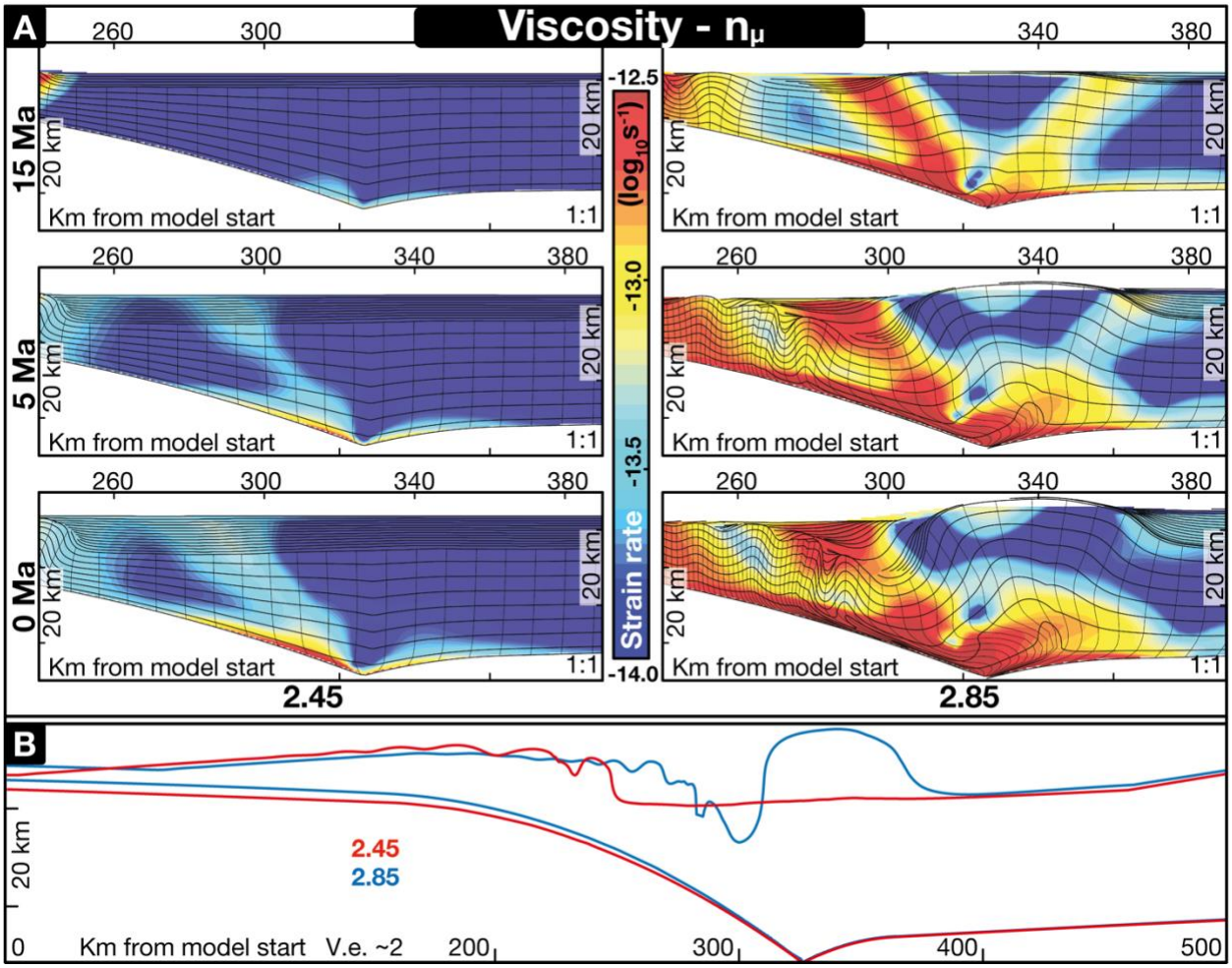

Figure 7. Variations in nμ. *Forearc high development with changes in the viscosity parameter nμ. A) The figure shows 15 Ma, 5 Ma, and 0 Ma snapshots of an inset of the model where the forearc high develops, for the models with 2.45 (left column) and 2.85 (right column). B) Line trace of the bottom of the crust and top of the basement in models with changes in the value of the viscosity parameter nμ after a complete run. We fix the "S" point as a reference to compare models.*

Within the parameter spectrum checked (Table 1), the activation energy, Q, influences the occurrence and shape of uplift in the forearc high. As expected, the effects of Q are reversed to those of n_μ. Relatively low values produce an uplift that is older and larger and occurs at earlier stages than in our Base Model. Uplift of a convex up area blocks the development of the initial forearc basin while inducing a second uplift in the model retro-wedge (Fig. 8). Surface uplift in the forearc high outpaces the primary subsidence, and uplift rates accelerate with time. Subsidence rates in the forearc lows to the sides of the forearc

high also accelerate with time. The width of the pro-basin decreases with time while that of the retro-basin increases until it stabilizes. Higher Q values accelerate the subsidence rates in the initial forearc basin, as the basin becomes slightly narrower (Fig. 8). Higher Q values lessen strain distribution and thus increase the stability of the margin, which tends to counteract the upward motion of a box-shaped area that takes place in the later stages of the simulations.

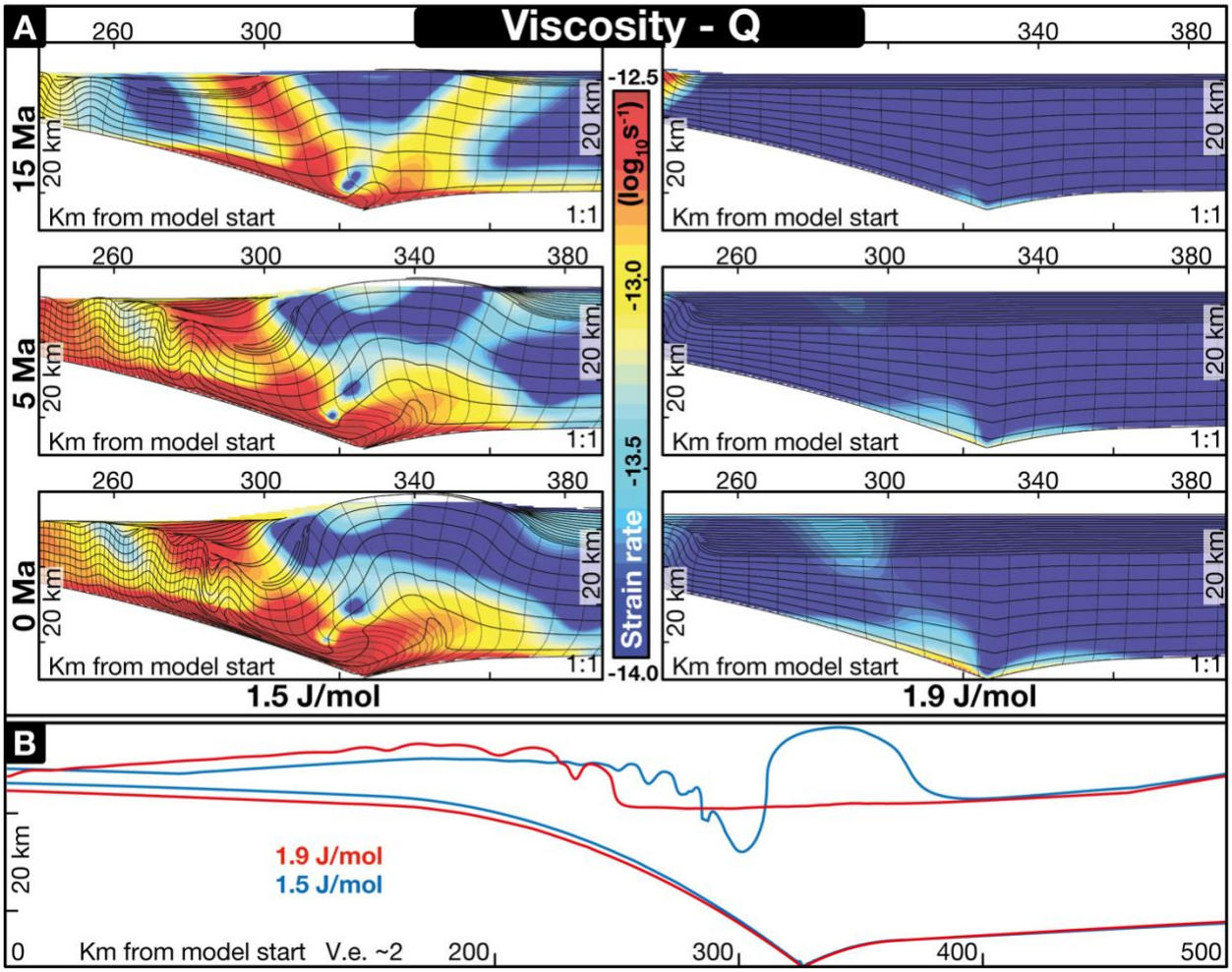

Figure 8. Variations in Q. *Forearc high development with changes in the viscosity parameter Q. A) The figure shows 15 Ma, 5 Ma, and 0 Ma snapshots of an inset of the model where the forearc high develops, for the models with 1.5 J/mol (left column) and 1.9 J/mol (right column). B) Line trace of the bottom of the crust and top of the basement in models with changes in the value of the viscosity parameter Q after a complete run. We fix the "S" point as a reference to compare models.*

5 Discussion

Models corroborate and detail the mechanism of forearc high uplift by deep crustal flow presented in Fernández-Blanco et al. (2020). Models show that margin sediment accretion and syn-accretion sedimentation in the forearc basin lead to higher temperatures at deeper levels of internal areas of orogenic wedges. Increased temperatures change the deformation mechanics in the lower crust from brittle to viscous. Thermal weakening of the lower crust results in ductile flow, and thickening and shortening of the wedge that leads to the dynamic growth of the forearc high if frontal accretion, and thus deformation, is sustained. Sedimentation rate in the forearc basin and the initial thermal and viscous state of the wedge control to a first order the timing and geometry of the preceding large-wavelength and subsequent short-wavelength vertical motions, i.e. forearc high uplift and coupled seaward subsidence.

5.1 Thermo-viscous uplift and forearc high formation

The subduction geometry sets the orogen cross-sectional shape at wedge front and the non-linear growth of topography at wedge rear. Along the convergence direction and sense, the orogen has a critical, positive-alpha topography from the trench to the trench-slope break, followed by a stable or critical negative-alpha topography at the front of a forearc high, that has a thermo-viscous, non-taper topography. When the accommodation space leading to a negative-alpha topography that is filled with sediments, a wide negative-alpha basin develops that halts strain in the underlying wedge and remains undeformed sliding above the decollement for as long as its depositional slope sets the wedge surface slope to zero (Fuller *et al.*, 2006a; Willett & Schlunegger, 2010). In the negative-alpha basin, sediment load and thermal resistivity contribute to increased temperatures and the activation of viscous flow in the lower crust, leading to shortening, thickening and uplift of a forearc high in the

rear of wedges under compression (Fernández-Blanco et al., 2020). A thermo-viscous forearc high has high strain rates and grows structurally independently of the wedge taper.

Our simulations suggest that forearc highs grow without lithological strength contrasts in the retro wedge of the model and by the geometrical characteristics of the wedge itself, ultimately a result of the landward dip increase of the slab. The same was postulated by Fuller et al. (2006a) for trench-slope breaks and forearc basins. The geometry and dip of the subducting slab control the point where the slab and the overriding plate become decoupled, and sets the location of the forearc high, developing above an area where no friction exerted by the subducting plate affect the overriding plate. Models show that the uplift of the forearc high occurs for a wide range of values of thermal conductivity (not shown in this contribution), viscosity, and sedimentation rate, and becomes more probable with time, as the forearc system enlarges and becomes more mature (Fernández-Blanco et al., 2020). The aforementioned inferences imply that forearc highs may not be considered an isolated feature conditioned to backstop presence (e.g., Byrne *et al.*, 1993), but rather an integral part of accretionary wedges that develop at advanced stages of wedge growth (e.g., Pavlis & Bruhn, 1983) as a function of the accretionary flux, initial wedge viscosity and synorogenic sedimentation.

Dynamic effects and feedbacks among several processes control the development of forearc highs without the need of a material-strength backstop in convergent orogens deforming during subduction by accretion of material into the overriding plate. The thermal structure of the deep wedge plays a key role that facilitate or hinder viscous deformation. If accretionary flux and convergence velocity are continuous and sufficient, a thermally activated viscosity drop at the base of the crust results in coupled, counteracting uplift and subsidence. Aside from sediment accretion, syn-accretion deposition and wedge viscosity are the two key parameters controlling the coupled, non-linear vertical motions that shape and time of growth of a forearc high.

5.2 Synorogenic sedimentation controls on forearc high formation

Variations in sedimentation rates significantly influence the growth of the margin (Fig. 5). Sedimentation rate and growth of the main forearc basin increase lower crust temperature by two processes; deposition of younger, colder sediments in the basin forces a vertical temperature gradient under them, much like a blanket, and thickens the crust, thus increasing the depth and temperature of its base. Both "thermal blanketing" and heating by overburden contribute to the progressive thermal activation of ductile strain in the lower crust and ultimately propels the growth of a forearc high. When sediment input is small, the development of structural highs along the margin takes place at high rates and at early stages of the simulations. A broad forearc high develops with small flanking basins (Fig. 5, left hand). As sedimentation increases, a long wavelength subsidence takes place at model initial stages and the onset of the forearc high growth is delayed (Fig. 5, right hand). Increasing sedimentation rate eventually leads to the absence of a forearc high, and protracted long wavelength subsidence.

Two counteracting effects compete during the growth of the forearc basin system: the thermal restrictions caused by the forearc basin sediments and their sedimentary load. Thermal upward circulation is restrained by the thermal resistivity or "blanketing" effect caused by the forearc basin sediments. Incoming sediments are colder than basement rocks, and therefore have lower heat transfer rates, which ultimately lead to higher temperatures underneath the forearc basin and a vertical thermal gradient. As the forearc basin thickens, increasingly higher temperatures set at the base of the crust. This leads to lower viscosities and thus lower resistance to deformation. Contrarily, larger sedimentary loads lead to larger isostatic subsidence. Since both effects act simultaneously, the sharper vertical gradients in temperature contributing to weakening in the lower crust, and thus promoting surface uplift of the forearc high, may be partially or completely masked due to regional subsidence and sediment load. These opposite controlling factors cause the region of the forearc basin to

undergo a sequenced downward-upward motion in which surface uplift of the forearc high takes place while subsidence in the surrounding areas persists in a relative frame. Also, the growth of the forearc high creates extra load and accommodation space in its adjacent basins.

Our models of accretionary margins show that if the amount of incoming sediments at the trench remains constant, variations in the sedimentation rate control the age and occurrence of surface uplift in the forearc high regions. Assuming an overfilled forearc basin in which the sediments available from the surrounding source areas outpace the accommodation space available, the amount of sediments that could potentially enter the system depends solely on subsidence. We thus reach the counterintuitive postulation that regional subsidence in the forearc basin can be the main cause behind surface uplift in the forearc high.

5.3 Initial wedge viscosity controls on forearc high formation

Variations in initial wedge viscosity markedly influence the growth of the margin (Fig. 6 to 8). Wedge viscosity and its thermally-controlled dynamic state leads to different degrees of strain localisation that in turn controls the occurrence, age, wavelength and rate of the motions in the wedge rear. Higher initial wedge viscosities (low A_μ, low n_μ, high Q) limit the viscous flow, delaying or masking the uplift of the forearc high, and lead to stable wedges that widen and thicken by sedimentation and subsidence in the forearc. On the contrary, under the same accretionary flux, lower initial wedge viscosities (high A_μ, high n_μ, low Q) facilitate ductile flow and the uplift of the forearc high by shortening and thickening. We thus infer that low viscosity at initial stages of wedge growth have similar effects as high temperatures in the evolution of the internal sectors of the wedge, and both parameters act as to anticipate and accelerate the morphologic evolution of mature wedges.

As already inferred by previous studies (Vanderhaeghe *et al.*, 2003), lowering the initial viscosity of the wedge results in larger decoupling of the lower crust, and increased extend of the viscous flow landwards. Our models further suggests that this effect is to a large extent controlled by syn-accretion sedimentation. Lower initial wedge viscosity results in a broader and more pronounced forearc high, sharply bounded by a seaward and a landward basin that continue to subside by sedimentary load. Sedimentation in these bounding forearc lows control the extent of viscous flow, and thus that of the uplift in the forearc high. Accommodation space in the negative-alpha basin at the front of the forearc high is controlled by the high in its proximal basin edge and by tectonic uplift of the slope-trench break in its distal basin edge (Willett & Schlunegger, 2010). On the contrary, accommodation space in the forearc basin at the back of the forearc high is solely controlled by the high. As a result, accommodation space increases at a faster pace in the seaward basin, in turn leading to an extra sedimentary load that translates the viscous flow of the lower crust farther landward. This effect, facilitated by lower viscosity and larger decouple of the negative-alpha region, increases the volume of viscously deforming rock and leading to lateral growth of the forearc high into a plateau.

5.4. Forearc high uplift in South Turkey and other settings

The analysis of the structures observed along the regional 2D geologic transect of the central Cyprus arc suggests shortening from the trench to south Turkey (Fig. 3). The type, distribution, relative age, and geometry of these contractional structures are compatible with their development in relation to a wide accretionary subduction system (e.g., Dickinson & Seely, 1979) (Figs. 1, 3). Simulations can reproduce the overall geometry and the main contact relationships as well as the main vertical tectonic events of the south Anatolian upper plate. These include early continuity and later disruption of Miocene basins in the presence of brittle, regional-scale accommodating structures in the seaward regions, i.e., the trench,

the trench-slope, and the trench-slope break areas, and broad monoclinal flexure above ductile strain in the otherwise largely undeformed landward forearc basin region (Figs. 3, 4), i.e. deformation lead by mechanical accretion at wedge shallower front and ductile strain at wedge deeper rear (e.g., Pavlis & Bruhn, 1983; Willett, 1992). In Central Cyprus, mechanical accretion dominates deformation in the Mesaoria Basin and the Kyrenia Range, while ductile deformation at deeper levels controls the growth of the Central Taurus Mountains, and thus the evolution of the basins of Cilicia and Mut (Fig. 1).

Data along the Central Cyprus subduction and our models suggest that the topography in the south of the Anatolian plate is driven by mechanical accretion from Cyprus and viscous deep-seated deformation in south Turkey (Fig. 9). South Turkey surface uplift and growth of the modern Central Taurus Mountains at ~8 Ma and later times (e.g., Cosentino *et al.*, 2012; Meijers *et al.*, 2018) and concomitant offshore subsidence (Walsh-Kennedy *et al.*, 2014) developed the monoclinal flexure of Miocene rocks (Fernández-Blanco *et al.*, 2019) as it divided the forearc basin into the landward uplifted Mut Basin, and the seaward subsided Cilicia Basin. Such coupled, short-wavelength vertical motions can be explained by the mechanism for thermo-viscous forearc high formation during the accretionary evolution of the Central Cyprus margin (Fernández-Blanco et al, 2020).

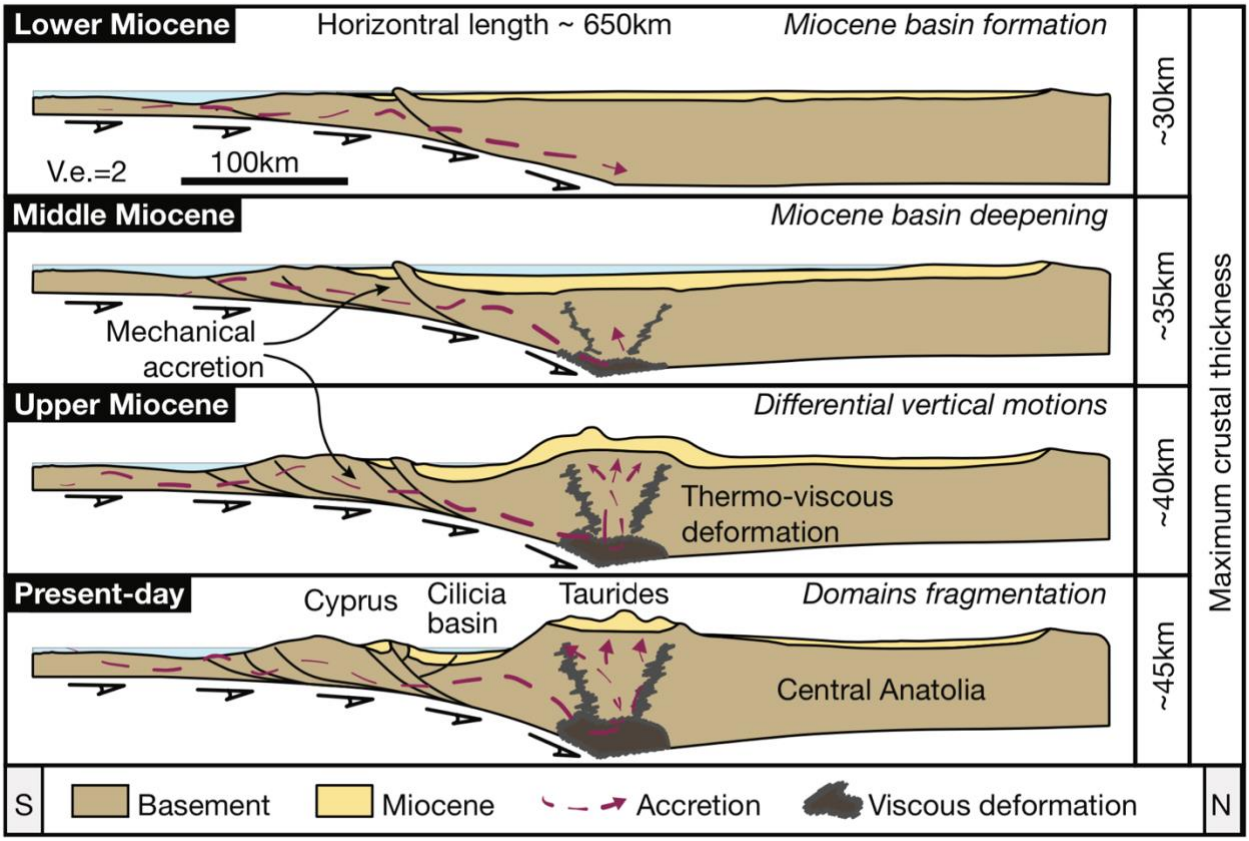

Figure 9. *Conceptual evolution of the Anatolian margin in Central Cyprus.*

Thermo-viscous forearc high evolution in relation to mechanical accretion is consistent with geologic observations along the margin. For example, the presence of Cyprus slab, as imaged by topography (e.g., Bakırcı *et al.*, 2012; Abgarmi *et al.*, 2017), is compatible with the location of the area of maximum crustal thicknesses and uplift (Fig. 3), hence solving the discrepancy inherent to slab break-off models (e.g., Schildgen *et al.*, 2014). Similarly, given that decreasing convergence velocity leads to orogenic collapse over a weak crustal base (Willett *et al.*, 1993), subduction locking in relation with the Eratosthenes Seamount explains the current extensional deformation of South Turkey. Low seismicity (Imprescia *et al.*, 2012) and the absence of accommodation structures (Fernández-Blanco *et al.*, 2019) along the uplifted area are observations also compatible with the thermo-viscous forearc high uplift of the modern Central Taurus Mountains.

The thermo-viscous forearc high uplift provides an explanation for the dynamically supported growth of broad, anomalously uplifted hinterland areas in other accretionary margins —Kodiak/Eastern Aleutian islands, in the Alaskan margin; Olympic Mts, in the Cascadia margin; Shikoku Island, in the Nankai margin—. These margins are mature, with forearc highs at >50 km of the trench-slope break and arc-trench gaps ~300 km, as already pointed by Pavlis & Bruhn (1983) as well for Markan and Lesser Antilles.

6. Conclusion

Our integration and interpretation of data in a transect along the Central Cyprus subduction suggest its evolution by subduction accretion since the Early Miocene. Simulations with 2D thermo-mechanical finite elements of accreting subduction wedges aimed at reproducing the first-order geology and vertical tectonic motions along the transect show that; (i) frictional-mechanical deformation sets the time sequence of structures and the topo-bathymetry in the trench, trench-of-slope and seaward areas of the forearc, and (ii) viscous-thermal deformation dominates in landward areas of the forearc and controls forearc high growth and its shape.

In our numerical models, the forearc high grows without a backstop, if a thermally-induced viscosity drop in the lower crust leads to weakening and ductile flow that is regulated by subduction accretion, shortening, and thickening. The occurrence, geometry, and timing of vertical motions associated with forearc high development vary in relation to the influence of sedimentation rate and viscosity in the resulting thermal and deformation state of the wedge. The margin stability increases when thicker basins develop in relation to higher sedimentation rates and higher viscosities. While low sedimentation rates lead to thin forearc basins and results in forearc high uplifting at earlier times of margin accretion, progressively higher sedimentation rates result in more pronounced basin thickening, delaying surface uplift. Similarly, lower viscosities produce prominent rounded-shaped

forearc highs developing at earlier model run times, while increasing viscosities result in uplift of an area that develops at progressively younger times and has an increasingly flatter and broader top surface. Very large sedimentation rates and/or higher viscosities stabilize the accretionary wedge and halt forearc high growth.

Models corroborate that ductile deformation, lead by thermally-activated viscosity at the base of the Anatolian crust and yielded by accretion of sediments incoming in the Cyprus Arc, is a viable mechanism driving the surface uplift that raised the modern Central Taurus Mountains. Our simulations reproduce upper plate deformation structures and modern sedimentary architectures along Central Cyprus and can be extrapolated to other accretionary margins with similar morphologies and vertical motions in time.

Acknowledgements

We thank the Netherlands Organisation for Scientific Research (NWO) for founding this study as a part of the Vertical Anatolian Movement Project (VAMP), a European Science Foundation (ESF) EuroCORE project within TOPOEurope. Authors have no conflict of interest. Data and models to reproduce the findings of this study are available from the corresponding author upon reasonable request.

References

Abgarmi, B., Delph, J.R., Arda Ozacar, A., Beck, S.L., Zandt, G., Sandvol, E., Turkelli, N. & Berk Biryol, C. (2017) Structure of the crust and African slab beneath the central Anatolian plateau from receiver functions: New insights on isostatic compensation and slab dynamics. *Geosphere* 13, 1774–1787.

Aksu, A.E., Calon, T.J., Hall, J., Mansfield, S. & Yaşar, D. (2005) The Cilicia–Adana basin complex, Eastern Mediterranean: Neogene evolution of an active fore-arc basin in an obliquely convergent margin. *Marine Geology* 221, 121–159.

Ates, A., Kearey, P. & Tufan, S. (1999) New gravity and magnetic anomaly maps of Turkey. *Geophysical Journal International* 136, 499–502.

Bakırcı, T., Yoshizawa, K. & Özer, M. (2012) Three-dimensional S-wave structure of the upper mantle beneath Turkey from surface wave tomography. *Geophysical Journal International* 190, 1058–1076.

Biryol, C., Beck, S.L., Zandt, G. & Özacar, A. (2011) Segmented African lithosphere beneath the Anatolian region inferred from teleseismic P-wave tomography. *Geophysical Journal International* 184, 1037–1057.

Byrne, D.E., Wang, W.-H. & Davis, D.M. (1993) Mechanical role of backstops in the growth of forearcs. *Tectonics* 12, 123–144.

Calon, T.J., Aksu, A.E. & Hall, J. (2005a) The Neogene evolution of the Outer Latakia Basin and its extension into the Eastern Mesaoria Basin (Cyprus), Eastern Mediterranean. *Marine Geology* 221, 61–94.

Calon, T.J., Aksu, A.E. & Hall, J. (2005b) The Oligocene-Recent evolution of the Mesaoria Basin (Cyprus) and its western marine extension, Eastern Mediterranean. *Marine Geology* 221, 95–120.

Cassola, T. (2013) Mechanics of forearc basins. ETH Zurich

Çıner, A., Karabiyikoğlu, M., Monod, O., Deynoux, M. & Tuzcu, S. (2008) Late Cenozoic Sedimentary Evolution of the Antalya Basin, Southern Turkey. *Turkish Journal of Earth Sciences* 17, 1–41.

Cosentino, D., Schildgen, T., Cipollari, P., Faranda, C., Gliozzi, E., Hudáčková, N., Lucifora, S. & Strecker, M.R. (2012) Late Miocene surface uplift of the southern margin of the Central Anatolian Plateau, Central Taurides, Turkey. *GSA Bulletin* 124, 133–145.

Dahlen, F.A. (1984) Noncohesive critical Coulomb wedges: An exact solution. *Journal of Geophysical Research* 89, 10125–10133.

Davis, D., Suppe, J. & Dahlen, F.A. (1983) Mechanics of fold-and-thrust belts and accretionary wedges. *Journal of Geophysical Research*.

DeCelles, P.G. & Giles, K.A. (1996) Foreland basin systems. *Basin Research* 8, 105–123.

Delph, J.R., Abgarmi, B., Ward, K.M., Beck, S.L., Arda Özacar, A., Zandt, G., Sandvol, E., Türkelli, N. & Kalafat, D. (2017) The effects of subduction termination on the continental lithosphere: Linking volcanism, deformation, surface uplift, and slab tearing in central Anatolia. *Geosphere* 13, 1788–1805.

Dickinson, W.R. & Seely, D.R. (1979) Structure and stratigraphy of forearc regions. *AAPG Bulletin* 63, 2–31.

Erdős, Z., Huismans, R.S. & van der Beek, P. (2015) First-order control of syntectonic sedimentation on crustal-scale structure of mountain belts. *Journal of Geophysical Research, [Solid Earth]* 120, 5362–5377.

Ergün, M., Okay, S., Sari, C., Zafer Oral, E., Ash, M., Hall, J. & Miller, H. (2005) Gravity anomalies of the Cyprus Arc and their tectonic implications. *Marine Geology* 221, 349–358.

Fernández-Blanco, D. (2014) Evolution of Orogenic Plateaus at Subduction Zones: Sinking and raising the southern margin of the Central Anatolian Plateau.

Fernández-Blanco, D., Bertotti, G., Aksu, A. & Hall, J. (2019) Monoclinal flexure of an orogenic plateau margin during subduction, south Turkey. *Basin Research* 13, 1774.

Fernández-Blanco, D., Bertotti, G. & Attila, Ç. (2013) Cenozoic tectonics of the Tuz Gölü Basin (Central Anatolia Plateau, Turkey). *Turkish Journal of Earth Sciences* 22, 715–738.

Fillon, C., Huismans, R.S. & van der Beek, P. (2013) Syntectonic sedimentation effects on the growth of fold-and-thrust belts. *Geology* 41, 83–86.

Forsyth, D.W. (1985) Subsurface loading and estimates of the flexural rigidity of continental lithosphere. *Journal of Geophysical Research* 90, 12623.

Fuller, C.W. (2006) Controls on the Structural Morphology and Subduction-thrust Seismicity of Accretionary Margins. University of Washington

Fuller, C.W., Willett, S.D. & Brandon, M.T. (2006a) Formation of forearc basins and their influence on subduction zone earthquakes. *Geology* 34, 65–68.

Fuller, C.W., Willett, S.D., Fisher, D. & Lu, C.Y. (2006b) A thermomechanical wedge model of Taiwan constrained by fission-track thermochronometry. *Tectonophysics* 425, 1–24.

Fullsack, P. (1995) An arbitrary Lagrangian-Eulerian formulation for creeping flows and its application in tectonic models. *Geophysical Journal International* 120, 1–23.

Imprescia, P., Pondrelli, S., Vannucci, G. & Gresta, S. (2012) Regional centroid moment tensor solutions in Cyprus from 1977 to the present and seismotectonic implications. *Journal of Seismology* 16, 147–167.

Jaupart, C. & Mareschal, J.C. (2005) Production from Heat Flow Data. *The Crust* 3, 65–84.

Koons, P.O. (1990) Two-sided orogen: Collision and erosion from the sandbox to the Southern Alps, New Zealand. *Geology* 18, 679–682.

Kopp, H. & Kukowski, N. (2003) Backstop geometry and accretionary mechanics of the Sunda margin. *Tectonics* 22.

Koulakov, I. & Sobolev, S.V. (2006) Moho depth and three-dimensional P and S structure of the crust and uppermost mantle in the Eastern Mediterranean and Middle East derived from tomographic inversion of local ISC data. *Geophysical Journal International* 164, 218–235.

Makris, J. & Stobbe, C. (1984) Physical properties and state of the crust and upper mantle of the Eastern Mediterranean Sea deduced from geophysical data. *Marine Geology* 55, 347–363.

Mart, Y. & Ryan, W.B.F. (2002) The complex tectonic regime of Cyprus arc: a short review. *Israel Journal of Earth Sciences* 51, 117–134.

McCay, G. (2010) Tectonic-sedimentary evolution of the Girne (Kyrenia) Range and the Mesarya (Mesaoria) Basin, North Cyprus. PhD. University of Edinburgh

Meijers, M.J.M., Brocard, G.Y., Cosca, M.A., Lüdecke, T., Teyssier, C., Whitney, D.L. & Mulch, A. (2018) Rapid late Miocene surface uplift of the Central Anatolian Plateau margin. *Earth and Planetary Science Letters* 497, 29–41.

Mutlu, A. & Karabulut, H. (2011) Anisotropic Pn tomography of Turkey and adjacent regions. *Geophysical Journal International* 187, 1743–1758.

Öğretmen, N., Cipollari, P., Frezza, V., Faranda, C., Karanika, K., Gliozzi, E., Radeff, G. & Cosentino, D. (2018) Evidence for 1.5 km of uplift of the Central Anatolian Plateau's southern margin in the last 450 kyr and implications for its multi-phased uplift history. *Tectonics*, 2017TC004805.

Özeren, M.S. & Holt, W.E. (2010) The dynamics of the eastern Mediterranean and eastern Turkey. *Geophysical Journal International* 183, 1165–1184.

Pavlis, T.L. & Bruhn, R.L. (1983) Deep-seated flow as a mechanism for the uplift of broad forearc ridges and its role in the exposure of high P/T metamorphic terranes. *Tectonics* 2, 473–497.

Platt, J.P. (1986) Dynamics of orogenic wedges and the uplift of high-pressure metamorphic rocks. *GSA*

Bulletin 97, 1037–1053.

Pope, D.C. & Willett, S.D. (1998) Thermal-mechanical model for crustal thickening in the central Andes driven by ablative subduction. *Geology* 26, 511–514.

Reilinger, R., McClusky, S., Vernant, P., Lawrence, S., Ergintav, S., Cakmak, R., Ozener, H., Kadirov, F., Guliev, I., Stepanyan, R., Nadariya, M., Hahubia, G., Mahmoud, S., Sakr, K., ArRajehi, A., Paradissis, D., Al-Aydrus, A., Prilepin, M., Guseva, T., Evren, E., Dmitrotsa, A., Filikov, S.V., Gomez, F., Al-Ghazzi, R. & Karam, G. (2006) GPS constraints on continental deformation in the Africa-Arabia-Eurasia continental collision zone and implications for the dynamics of plate interactions: Eastern Mediterranean active tectonics. *Journal of Geophysical Research* 111.

Robertson, A.H.F. (1998) Mesozoic-Tertiary tectonic evolution of the easternmost Mediterranean area: integration of marine and land evidence. *Proceedings of the Ocean Drilling Program. Scientific results Ocean Drilling Program*.

Schildgen, T.F., Yıldırım, C., Cosentino, D. & Strecker, M.R. (2014) Linking slab break-off, Hellenic trench retreat, and uplift of the Central and Eastern Anatolian plateaus. *Earth-Science Reviews* 128, 147–168.

Smit, J.H.W., Brun, J.P. & Sokoutis, D. (2003) Deformation of brittle-ductile thrust wedges in experiments and nature. *Journal of geophysical research* 108, 3.

Stephenson, R.A., Mart, Y., Okay, A., Robertson, A., Saintot, A., Stovba, S. & Khriachtchevskaia, O. (2004) TRANSMED Transect VIII: Eastern European Craton--Crimea--Black Sea--Anatolia--Cyprus--Levant Sea--Sinai--Red Sea. *The TRANSMED Atlas: The Mediterranean Region from Crust to Mantle*, 120–127.

Vanderhaeghe, O., Medvedev, S., Fullsack, P., Beaumont, C. & Jamieson, R.A. (2003) Evolution of orogenic wedges and continental plateaux: insights from crustal thermal–mechanical models overlying subducting mantle lithosphere. *Geophysical Journal International* 153, 27–51.

Walsh-Kennedy, S., Aksu, A.E., Hall, J., Hiscott, R.N., Yaltırak, C. & Çifçi, G. (2014) Source to sink: The development of the latest Messinian to Pliocene–Quaternary Cilicia and Adana Basins and their linkages with the onland Mut Basin, eastern Mediterranean. *Tectonophysics* 622, 1–21.

Willett, S., Beaumont, C. & Fullsack, P. (1993) Mechanical model for the tectonics of doubly vergent compressional orogens. *Geology* 21, 371–374.

Willett, S.D. (1992) Dynamic and kinematic growth and change of a Coulomb wedge. In: K. R. McClay (Ed), *Thrust Tectonics*. Springer Netherlands, Dordrecht, pp. 19–31.

Willett, S.D. (1999) Orogeny and orography: The effects of erosion on the structure of mountain belts. *Journal of geophysical research* 104, 28957–28981.

Willett, S.D. & Schlunegger, F. (2010) The last phase of deposition in the Swiss Molasse Basin: from foredeep to negative-alpha basin. *Basin Research* 22, 623–639.

Figures & Table

Figure 1. Accretionary margins in nature and models. Main morphotectonic features in **(A)** a generic accretionary margin with forearc high, in **(B)** models of subduction wedge accretion, and **(C)** their correlation to features in Central Cyprus. For natural examples, we use original definitions by Karig & Sharman (1975) and Dickinson & Seely (1979), and for numerical models a simpler nomenclature (e.g., Fuller, 1996). "Trench-fill basin" and "accretionary forearc basin" are que nature equivalents to "pro-wedge" and "wedge-top" basins in models, and the terms "residual" and "intramassif forearc basins" of Dickinson & Seely (1979) are in simulations the "landward" and "seaward" forearc basins, respectively. Correlation with elements along the Central Cyprus margin is based in Fernández-Blanco et al., 2020.

Figure 2. Model setup. Model setup, with an indication of thermal and mechanical parameters.

Figure 3. Transects along the Anatolian maring in Central Cyprus. Upper-crust and crustal-scale geological transects running N-S (650 km at around 33°30' E). The transects stretch from the Levantine Basin to the Tuz Gölü Basin across the Cyprus arc-trench, the island of Cyprus, the Cilicia Basin, the Central Taurus Mountains, and the Central Anatolian interior. The upper-left panel is a location map. Panel A is a transect across Central Cyprus and Anatolia, simplified from Stephenson et al. (2004), that has a topo-bathymetry with 3 times vertical exaggeration. EMed = East Mediterranean; CTM = Central Taurus Mountains; TGB = Tuz Golu Basin; CPM = Central Pontides Mountains; BkS = Black Sea. Panel B is the upper sector of the transect (up to 10 km depth), shown with ~7 km of vertical exaggeration, and Panel C is the crustal cross-section for the area. These transects integrate upper crustal studies (Robertson, 1998; Stephenson *et al.*, 2004; Calon *et al.*, 2005a, 2005b; Çıner *et al.*,

2008; McCay, 2010; Fernández-Blanco *et al.*, 2013) with the interpretation of several geophysical studies (Ates *et al.*, 1999; Mart & Ryan, 2002; Ergün *et al.*, 2005; Koulakov & Sobolev, 2006; Özeren & Holt, 2010; Mutlu & Karabulut, 2011; Abgarmi *et al.*, 2017; Delph *et al.*, 2017), as detailed in Fernández-Blanco (2014). CVP = Central Volcanic Province.

Figure 4. Base Model. Mechanical model evolution in time steps, with zoom-ins into the area where the forearc high develops. Times represented are, from top to bottom: 25Ma, 15Ma, 10Ma, 5Ma, and present. The individual lines on top of the basement represent isochrones and should reflect the overall geometric relationships expected for strata.

Figure 5. Variations in sedimentation rates. Forearc high development with changes in sedimentation rates. A) The figure shows 15 Ma, 5 Ma, and 0 Ma snapshots of an inset of the model where the forearc high develops, for the models with 0.1 mm/y (left column) and 0.9 mm/y (right column). B) Line trace of the bottom of the crust and top of the basement in models with changes in sedimentation rates after a complete run. We fix the "S" point as a reference to compare models.

Figure 6. Variations in A_μ. Forearc high development with changes in the viscosity pre-exponential parameter A_μ. A) The figure shows 15 Ma, 5 Ma, and 0 Ma snapshots of an inset of the model where the forearc high develops, for the models with 0.75 Pa^{-n}/Ma (left column) and 3.45 Pa^{-n}/Ma (right column). B) Line trace of the bottom of the crust and top of the basement in models with changes in the value of the viscosity parameter A_μ after a complete run. We fix the "S" point as a reference to compare models.

Figure 7. Variations in n_μ. Forearc high development with changes in the viscosity parameter n_μ. A) The figure shows 15 Ma, 5 Ma, and 0 Ma snapshots of an inset of the model

where the forearc high develops, for the models with 2.45 (left column) and 2.85 (right column). B) Line trace of the bottom of the crust and top of the basement in models with changes in the value of the viscosity parameter n_μ after a complete run. We fix the "S" point as a reference to compare models.

Figure 8. Variations in Q. Forearc high development with changes in the viscosity parameter Q. A) The figure shows 15 Ma, 5 Ma, and 0 Ma snapshots of an inset of the model where the forearc high develops, for the models with 1.5 J/mol (left column) and 1.9 J/mol (right column). B) Line trace of the bottom of the crust and top of the basement in models with changes in the value of the viscosity parameter Q after a complete run. We fix the "S" point as a reference to compare models.

Figure 9. Conceptual evolution of the Anatolian margin in Central Cyprus.

Table 1. Values of the main parameters used in the Base Model and their parameterization for the suites of viscosity and sedimentation rate.

Supplementary material

Suppl. Material A. Model Design, formulation and routines.

Accretion mechanisms at accretionary margins are often described using the critical wedge theory (Davis et al., 1983; Dahlen, 1984; Larroque et al., 1995; Malavieille, 2010), which defines the geometry of the orogenic wedge as a function of the mechanical properties of the accreting wedge and that of its surface of accretion. However, the critical wedge excludes the ductile properties of these systems, such as the absence of brittle fracturing in their lower ends, which cause relevant deviations from the predicted brittle morphologies. Recent research inclusive of visco-plastic attributes show the influence of thermal or rheological variations or that of sediment load and/or competence in the strain distribution and deformation patterns within the accretionary wedge (e.g., Fuller et al., 2006; Willett and Schlunegger, 2010; Simpson, 2010; Fillon et al., 2013).

We used the coupled mechanical-thermal model of collisional wedges modified to account for features associated with a subduction wedge used in previous studies (Willett, 1992; Willett and Pope, 2004; Fuller et al., 2006). Our 2D kinematic-dynamic models consist of two coupled domains (Fig. DR2). The domain where mechanical laws apply represents the crust of a deforming subduction zone. Accretion of incoming sediments is driven by the tangential velocities at the base of the mechanical domain. These velocities decrease toward, and become zero at, the "S" point, which represents the point of contact of the subducting slab and the continental Moho. The thermal domain covers the whole model, including the mechanical domain.

The model is consistent with time and cross-sectional lengths of interest and

simulates 25Ma of subduction in a transect of 550 km (Fig. 1). Parameters such as amount of material incoming at the trench and convergence velocity are set constant during the simulations. We adopted values of 3 km and 35 mm/y, respectively, which are considerably lower than present for the incoming material at the trench and higher than present for the convergence velocities. Our choice is based on the needed extrapolation in time (25Ma) of present-day values. The present day sedimentary thicknesses in the East Mediterranean Sea range from 10 km to 15 km (e.g., Makris and Stobbe, 1984); these values are probably the largest along the time frame of interest, considering factors such as the narrower confinement of the present-day Mediterranean or the presence of the Nile. Similarly, the under-thrust of the Erastothenes Seamount below South Cyprus presently decelerates subduction motion to 9. 3 ± 0. 3 mm/y (Reilinger et al., 2006), thus a larger, more common, convergence velocity value is given for the time considered for our simulations.

The subducting lithosphere is 50 My old at the left side of the model and its 70 km thickness remains constant during the running time. Since thicknesses in the mechanical domain, which represents the crust, change as accretion takes place, an initial thickness of 30 km is chosen on the basis of the similarity between thicknesses in nature and in models after the run is completed, i.e., maximum values of 45 km near the "S" point. The rest of the overriding lithosphere is 80 km thick. Flexural rigidity is set at 2.4×10^{23} N-m for both plates (after Fuller, 1996). Variations of this value of up to four orders magnitude did not produce substantial changes (e.g., Forsyth, 1985 for a discussion on flexural rigidity values). Densities are commonly accepted values: 2.8 g/cc for the lithosphere (which includes the sedimentary cover), 3.3 g/cc for the mantle and 1.03 g/cc for the overlying layer of water. Cohesion and internal friction angles control the mechanical strengths in our model. Cohesion, *c*, is set to

1000 Pa, a value higher than expected for the crust, to maintain model stability. Lower values do not affect the outcomes (Fuller, 1996).

The internal friction angle of the crustal material, φ, is set to 27° and the friction angle between the subducting and the overriding plates, φ_b, to 8°. Friction values are set low to include the effect of fluid pressures, not explicitly taken into account, and imply fluid pressure ratios within the range of those at accretionary wedges (Fuller, 1996, and the references therein).

To let the thermal structure equilibrate, the thermal model runs for 20 My before the crustal model onsets. Surface temperature is 5 °C, an average between subaerial and subaquatic temperatures, and a value of 1400 °C is given for the asthenosphere at the base of the model. We use values for thermal conductivity of 2 and 50 W/(m·°K) for the lithosphere and the asthenosphere. Asthenospheric conductivity values are readably high to represent isothermal conditions. Heat production has a value of 0. 85 μW/ m3 (Jaupart and Mareschal, 2005), occurring only in the mechanical domain. Specific heat, c, is 1200 J/ kg°·K for both model domains.

Boundary conditions

The simulation is governed by boundary conditions on velocity and frictional stick-slip along the domain limits. The plates converge by an horizontal velocity, v_c, which is set in the left side of the model, while the right side is fixed in space. The "S" point, being the intersection point where the subducting slab meets the continental Moho, divides a left domain with a frictional stick-slip boundary condition, and a right domain with a zero tangential velocity boundary condition.

This set of boundary conditions allows the calculation of the slip in the interface between the subducting and overriding plates. This slip depends on the shear stress at the plate interface, τ, and the shear strength of the interface, τ_c, defined as:

$$\tau_c = \sigma_n \tan(\varphi_b), \quad (1)$$

where σ_n and φ_b are the normal force and friction angles at the plate interface, respectively. No slip at the interface occurs when $\tau < \tau_c$ and the overlying material is then "locked". Contrarily, if $\tau > \tau_c$ slip occurs. The amount of slip is found iteratively by applying $\tau = \tau_c$, i.e. the shear stress on the interface equals the shear strength. These boundary conditions entails the off-interface remaining at v_c to drive the deformation within the model.

Relevant subroutines

Flexural isostasy. Elastic deformation is excluded from the mechanical model and elastic plate flexure is explicitly included for the entire model. The plates respond isostatically to crustal loads by vertical motions, in which the deflection of the plate is calculated analytically. That is, the weight of the crust is applied as a load on both plates, which behave as semi-infinite, or broken, elastic plates (Hetényi and Hetbenyi, 1946) coupled at the "S" point to ensure their contact. Thus, the flexural rigidity of the plates and the density of the mantle, crust, and water layer, control the flexural response in both plates (Fuller, 1996).

Sedimentation. Submarine sedimentation is simulated at the upper surface of all models. The model assumes that sediments are abundant and have the same material properties as the rest of the crust. Sedimentation takes place instantaneously from sources that are not within the model, first filling the accommodation space provided by the closed depressions,

which eventually fills completely, leading to overfilled basins and by-pass of sediments ("fill-to-spill"). Filling within the basins occurs from the lowest point by advection of points as a function of the inputted accumulation rate (Cassola, 2013).

Thermal state. In the thermal domain, the temperature is computed using a finite element method that solves the advective-conductive heat transfer equation with radiogenic heat production:

$$\varrho c_p \frac{\alpha T}{\alpha t} = \frac{\alpha}{\alpha x}\left(k \frac{\alpha T}{\alpha x}\right) + \frac{\alpha}{\alpha z}\left(k \frac{\alpha T}{\alpha z}\right) - \varrho c_p v_x \frac{\alpha T}{\alpha z} - \varrho c_p v_z \frac{\alpha T}{\alpha z} + A, \quad (2)$$

in which ϱ is the density, c_p the specific heat, T the temperature, t the time, k the thermal conductivity, and v_x and v_z are the horizontal and vertical components of the velocity, respectively. The velocities in the remaining regions are assigned kinematically to ensure the conservation of heat and mass within the model domain. Heat production is included in a layer of thickness d_a, representing the region of the highest concentration of radiogenic elements in the crust. In the upper and lower surfaces, constant temperature boundary conditions are used, with the exception of the area where the subduction lithosphere reaches the base of the model. This area as well as the sides of the model have no heat flux. To simulate the thermal pre-collision situation in the subduction zone, the thermal model runs for a certain amount of time, t_{runup}, with a steady initial velocity field.

Suppl. Material B. Model Videos.

Suppl. Material C. Regional Transect from the Mediterranean to Anatolia

We reconstruct a transect spanning from the East Mediterranean to the Central Anatolian Plateau interior.

To reproduce uppermost crustal structures and the geometry of Miocene and younger rocks (Fig. 3C), we integrate own findings (Fernández-Blanco, 2014) with published data in regional studies (Robertson, 1998a, 1998b; Stephenson et al., 2004; Harrison et al., 2004; Calon et al., 2005a, 2005b; Çıner et al., 2008; Fernández-Blanco et al., 2013, 2018; McCay et al., 2013). We assembled the interpretations of each area as shown originally in their sources, and the reader is referred there for details.

To constrain the geometry of the bottom of the crust and that of the Cyprus slab, we interpreted geophysical data from (Ergün et al., 2005; Koulakov and Sobolev, 2006; Mutlu & Karabulut, 2011; Özeren & Holt, 2010) and others, as shown in detail in Fernández-Blanco 2014, and integrate it with the TransMED transect VII (Stephenson et al., 2004). We also used constraints from Bakırcı et al. (2012) and Biryol et al. (2011) as appropriate.

References

Bakırcı, T., Yoshizawa, K., and Özer, M., 2012, Three-dimensional S-wave structure of the upper mantle beneath Turkey from surface wave tomography: Geophysical Journal International, v. 190, p. 1058–1076.

Biryol, C., Beck, S.L., Zandt, G., and Özacar, A., 2011, Segmented African lithosphere beneath the Anatolian region inferred from teleseismic P-wave tomography: Geophysical Journal International, v. 184, p. 1037–1057.

Calon, T.J., Aksu, A.E., and Hall, J., 2005a, The Neogene evolution of the Outer Latakia Basin and its extension into the Eastern Mesaoria Basin (Cyprus), Eastern Mediterranean: Marine Geology, v. 221, p. 61–94.

Calon, T.J., Aksu, A.E., and Hall, J., 2005b, The Oligocene-Recent evolution of the Mesaoria Basin (Cyprus) and its western marine extension, Eastern Mediterranean: Marine Geology, v. 221, p. 95–120.

Cassola, T. (2013). Mechanics of Forearc Basins. PhD thesis, Eidgenossiche Technische Hochschule (ETH).

Çıner, A., Karabiyikoğlu, M., Monod, O., Deynoux, M., and Tuzcu, S., 2008, Late Cenozoic Sedimentary Evolution of the Antalya Basin, Southern Turkey: Turkish Journal of Earth Sciences, v. 17.

Dahlen, F.A., 1984, Noncohesive critical Coulomb wedges: An exact solution: Journal of Geophysical Research, v. 89, p. 10125–10133.

Davis, D., Suppe, J., and Dahlen, F.A., 1983, Mechanics of fold-and-thrust belts and accretionary wedges: Journal of geophysical research, http://onlinelibrary.wiley.com/doi/10.1029/JB088iB02p01153/full.

Ergün, M., Okay, S., Sari, C., Zafer Oral, E., Ash, M., Hall, J., and Miller, H., 2005, Gravity anomalies of the Cyprus Arc and their tectonic implications: Marine Geology, v. 221, p. 349–358.

Fernandez-Blanco, D., 2014, Evolution of Orogenic Plateaus at Subduction Zones: Sinking and raising the southern margin of the Central Anatolian Plateau: PhD thesis, Amsterdam: Vrije Universiteit, http://dare.ubvu.vu.nl/bitstream/handle/1871/52042/end?sequence=3.

Fernández-Blanco, D., Bertotti, G., Aksu, A., and Hall, J., 2018, Miocene monocline flexure formed the Central Anatolian Plateau southern margin:, Earth ArXiv doi: 10.17605/OSF.IO/KS6RG.

Fernández-Blanco, D., G., B., and and Attila, Ç., 2013, Cenozoic tectonics of the Tuz Gölü Basin (Central Anatolia Plateau, Turkey): Turkish Journal of Earth Sciences, v. 22, p. 715–738.

Fillon, C., Huismans, R.S., van der Beek, P., and Muñoz, J.A., 2013, Syntectonic sedimentation controls on the evolution of the southern Pyrenean fold-and-thrust belt: Inferences from coupled tectonic-surface processes models: Modeling of the Southern Pyrenean FTB: Journal of Geophysical Research: Solid Earth, v. 118, p. 5665–5680.

Forsyth, D.W., 1985, Subsurface loading and estimates of the flexural rigidity of continental lithosphere: Journal of Geophysical Research, v. 90, p. 12623.

Fuller, C.W. (1996). Controls on the Structural Morphology and Subduction Thrust Seismicity of Accretionary Margins. PhD thesis, University of Washington.

Fuller, C.W., Willett, S.D., and Brandon, M.T., 2006, Formation of forearc basins and their influence on subduction zone earthquakes: Geology, v. 34, p. 65–68.

Harrison, R.W., Newell, W.L., Batıhanlı, H., Panayides, I., McGeehin, J.P., Mahan, S.A., Őzhűr, A., Tsiolakis, E., and Necdet, M., 2004, Tectonic framework and Late Cenozoic tectonic history of the northern part of Cyprus: implications for earthquake hazards and regional tectonics: Journal of Asian Earth Sciences, v. 23, p. 191–210.

Hetényi, M. and Hetbenyi, M. I. (1946). Beams on elastic foundation: theory with applications in the fields of civil and mechanical engineering, volume 16. University of Michigan Press.

Jaupart, C., and Mareschal, J.C., 2005, Production from Heat Flow Data: The crust, v. 3, p. 65–84.

Koulakov, I., and Sobolev, S.V., 2006, Moho depth and three-dimensional P and S structure of the crust and uppermost mantle in the Eastern Mediterranean and Middle East derived from tomographic inversion of local ISC data: Geophysical Journal International, v. 164, p. 218–235.

Larroque, C., Calassou, S., Malavieille, J., and Chanier, F., 1995, Experimental modelling of forearc basin development during accretionary wedge growth: Basin Research, v. 7, p. 255–268.

Luccio, F., and Pasyanos, M.E., 2007, Crustal and upper-mantle structure in the Eastern Mediterranean from the analysis of surface wave dispersion curves: Geophysical Journal International, v. 169, p. 1139–1152.

Makris, J., and Stobbe, C., 1984, Physical properties and state of the crust and upper mantle of the Eastern

Mediterranean Sea deduced from geophysical data: Marine Geology, v. 55, p. 347–363.

Malavieille, J., 2010, Impact of erosion, sedimentation, and structural heritage on the structure and kinematics of orogenic wedges: Analog models and case studies: GSA Today, v. 20, p. 4–10.

McCay, G.A., Robertson, A.H.F., Kroon, D., Raffi, I., Ellam, R.M., and Necdet, M., 2013, Stratigraphy of Cretaceous to Lower Pliocene sediments in the northern part of Cyprus based on comparative 87 Sr/86 Sr isotopic, nannofossil and planktonic foraminiferal dating: Geological Magazine, v. 150, p. 333–359.

Mutlu, A.K., and Karabulut, H., 2011, Anisotropic Pn tomography of Turkey and adjacent regions: Geophysical Journal International, https://academic.oup.com/gji/article-abstract/187/3/1743/618417.

Özeren, M.S., and Holt, W.E., 2010, The dynamics of the eastern Mediterranean and eastern Turkey: Geophysical Journal International, v. 183, p. 1165–1184.

Reilinger, R., McClusky, S., Vernant, P., Lawrence, S., Ergintav, S., Cakmak, R., Ozener, H., Kadirov, F., Guliev, I., Stepanyan, R., Nadariya, M., Hahubia, G., Mahmoud, S., Sakr, K., et al., 2006, GPS constraints on continental deformation in the Africa-Arabia-Eurasia continental collision zone and implications for the dynamics of plate interactions: EASTERN MEDITERRANEAN ACTIVE TECTONICS: Journal of Geophysical Research, v. 111, doi: 10.1029/2005JB004051.

Robertson, A.H.F., 1998a, Mesozoic-Tertiary tectonic evolution of the easternmost Mediterranean area: integration of marine and land evidence: Proceedings of the Ocean Drilling Program, Scientific Results, Vol. 160; Chapter 54, http://www.era.lib.ed.ac.uk/handle/1842/559.

Robertson, A.H.F., 1998b, Tectonic significance of the Eratosthenes Seamount: a continental fragment in the process of collision with a subduction zone in the eastern Mediterranean (Ocean Drilling Program Leg 160): Tectonophysics, v. 298, p. 63–82.

Simpson, G.D.H., 2010, Formation of accretionary prisms influenced by sediment subduction and supplied by sediments from adjacent continents: Geology, v. 38, p. 131–134.

Stephenson, R.A., Mart, Y., Okay, A., Robertson, A., Saintot, A., Stovba, S., and Khriachtchevskaia, O., 2004, TRANSMED Transect VIII: Eastern European Craton--Crimea--Black Sea--Anatolia--Cyprus--Levant Sea--Sinai--Red Sea: The TRANSMED Atlas: The Mediterranean Region from Crust to Mantle, p. 120–127.

Willett, S.D., 1992, Dynamic and kinematic growth and change of a Coulomb wedge, *in* McClay, K.R. ed., Thrust Tectonics, Dordrecht, Springer Netherlands, p. 19–31.

Willett, S.D., and Pope, D.C., 2004, Thermo-mechanical models of convergent orogenesis: thermal and rheologic dependence of crustal deformation: Rheology and Deformation of the Lithosphere at Continental Margins. Columbia University Press, New York, NY, p. 179–222.

Willett, S.D., and Schlunegger, F., 2010, The last phase of deposition in the Swiss Molasse Basin: From foredeep to negative-alpha basin: Basin Research, v. 22, p. 623–639.